Mimicking the mechanical properties of cortical bone with an additively manufactured biodegradable Zn-3Mg alloy

Zheng, Yuzhe; Huang, Chengcong; Li, Yageng; Gao, Jiaqi; Yang, Yabin; Li, Weishi; Zhou, Jie; Zadpoor, Amir A.; Wang, Luning; More Authors

DOI
10.1016/j.actbio.2024.05.023

Publication date
2024

Document Version
Final published version

Published in
Acta Biomaterialia

Citation (APA)
Zheng, Y., Huang, C., Li, Y., Gao, J., Yang, Y., Li, W., Zhou, J., Zadpoor, A. A., Wang, L., & More Authors (2024). Mimicking the mechanical properties of cortical bone with an additively manufactured biodegradable Zn-3Mg alloy. *Acta Biomaterialia*, *182*, 139-155. https://doi.org/10.1016/j.actbio.2024.05.023

Acta Biomaterialia 182 (2024) 139–155

Contents lists available at ScienceDirect

Acta Biomaterialia

journal homepage: www.elsevier.com/locate/actbio

Full length article

Mimicking the mechanical properties of cortical bone with an additively manufactured biodegradable Zn-3Mg alloy

Yuzhe Zheng[a,1], Chengcong Huang[a,1], Yageng Li[a,b,*], Jiaqi Gao[a], Youwen Yang[c], Shangyan Zhao[a], Haodong Che[a], Yabin Yang[d], Shenglian Yao[a], Weishi Li[e,f,g], Jie Zhou[h], Amir A. Zadpoor[h], Luning Wang[a,b,*]

[a] *Beijing Advanced Innovation Center for Materials Genome Engineering, School of Materials Science and Engineering, University of Science and Technology Beijing, 30 Xueyuan Road, Haidian District, Beijing, 100083, China*
[b] *Institute of Materials Intelligent Technology, Liaoning Academy of Materials, Shenyang, 110004, China*
[c] *Institute of Additive Manufacturing, Jiangxi University of Science and Technology, Nanchang 330013, China*
[d] *School of Materials Science and Engineering, Sun Yat-Sen University, Guangzhou 510275, China*
[e] *Department of Orthopaedics, Peking University Third Hospital, No. 49 NorthGarden Road, Haidian District, Beijing, 100191, China*
[f] *Beijing Key Laboratory of Spinal Disease Research, Beijing, 100191, China*
[g] *Engineering Research Center of Bone and Joint Precision Medicine, Ministry of Education, Beijing, 100191, China*
[h] *Department of Biomechanical Engineering, Delft University of Technology, Delft 2628 CD, the Netherlands*

ARTICLE INFO

Article history:
Received 1 December 2023
Revised 3 May 2024
Accepted 9 May 2024
Available online 13 May 2024

Keywords:
Laser powder bed fusion
Zinc alloy
Mechanical properties
Degradation behavior
Biocompatibility

ABSTRACT

Additively manufactured (AM) biodegradable zinc (Zn) alloys have recently emerged as promising porous bone-substituting materials, due to their moderate degradation rates, good biocompatibility, geometrically ordered microarchitectures, and bone-mimicking mechanical properties. While AM Zn alloy porous scaffolds mimicking the mechanical properties of trabecular bone have been previously reported, mimicking the mechanical properties of cortical bone remains a formidable challenge. To overcome this challenge, we developed the AM Zn-3Mg alloy. We used laser powder bed fusion to process Zn-3Mg and compared it with pure Zn. The AM Zn-3Mg alloy exhibited significantly refined grains and a unique microstructure with interlaced α-Zn/Mg_2Zn_{11} phases. The compressive properties of the solid Zn-3Mg specimens greatly exceeded their tensile properties, with a compressive yield strength of up to 601 MPa and an ultimate strain of $>$60 %. We then designed and fabricated functionally graded porous structures with a solid core and achieved cortical bone-mimicking mechanical properties, including a compressive yield strength of $>$120 MPa and an elastic modulus of $\approx$20 GPa. The biodegradation rates of the Zn-3Mg specimens were lower than those of pure Zn and could be adjusted by tuning the AM process parameters. The Zn-3Mg specimens also exhibited improved biocompatibility as compared to pure Zn, including higher metabolic activity and enhanced osteogenic behavior of MC3T3 cells cultured with the extracts from the Zn-3Mg alloy specimens. Altogether, these results marked major progress in developing AM porous biodegradable metallic bone substitutes, which paved the way toward clinical adoption of Zn-based scaffolds for the treatment of load-bearing bony defects.

Statement of significance

Our study presents a significant advancement in the realm of biodegradable metallic bone substitutes through the development of an additively manufactured Zn-3Mg alloy. This novel alloy showcases refined grains and a distinctive microstructure, enabling the fabrication of functionally graded porous structures with mechanical properties resembling cortical bone. The achieved compressive yield strength and elastic modulus signify a critical leap toward mimicking the mechanical behavior of load-bearing bone.

---

[*] Corresponding authors.
E-mail addresses: yagengli@ustb.edu.cn (Y. Li), luning.wang@ustb.edu.cn (L. Wang).
[1] Authors contributed equally.

https://doi.org/10.1016/j.actbio.2024.05.023

Moreover, our findings reveal tunable biodegradation rates and enhanced biocompatibility compared to pure Zn, emphasizing the potential clinical utility of Zn-based scaffolds for treating load-bearing bony defects. This breakthrough opens doors for the wider adoption of zinc-based materials in regenerative orthopedics.

1. Introduction

Treatment of large bony defects, arising from trauma, infections, bone tumors, or congenital anomalies, presents significant challenges in orthopedics. These defects cannot heal naturally, necessitating bone grafting [1]. While autologous grafts are considered the gold standard because of their optimal osteogenesis, osteoinduction, osteoconduction, and low risk of immunological rejection, they have several drawbacks, including the needs for multiple surgeries, surgical complications, and donor-site morbidity. In recent years, there has been growing interest in developing safe and effective artificial bone substitutes [2].

Among bone-substituting materials, metals offer superior mechanical properties as compared to polymers and ceramics. Bio-inert metals, such as titanium (Ti) and its alloys [3] as well as cobalt-chromium (CoCr) alloys [4], are widely used in orthopedics due to their high strengths and biocompatibility. However, the mismatch in elastic modulus with human bone can lead to stress shielding [5], negatively affecting the quality of the surrounding bone, implant stability, and durability [6]. Moreover, bio-inert implants unnecessarily retained in the human body may lead to inflammatory responses or implant-associated infections [1], and may require a second surgery. Biodegradable metals offer the possibility to provide initial mechanical support while gradually degrading in the human body during the healing process, thereby overcoming the drawbacks of bio-inert metals [7].

Zinc (Zn) with a moderate degradation rate and good biocompatibility is considered to be one of the promising biodegradable metals [8]. More importantly, Zn plays a pivotal role in the metabolic activity of various cells, promoting bone regeneration by positively affecting chondrocyte and osteoblast functions while inhibiting osteoclast activity [9]. However, Zn has a relatively low mechanical strength, with conventionally produced solid zinc exhibiting a tensile strength 28–120 MPa, which is comparable to the strengths of trabecular bone but far below those of cortical bone [10]. Alloying Zn is an effective strategy to achieve cortical bone-like strengths.

Recent progress in additive manufacturing (AM) has presented unprecedented opportunities for the development of ideal bone substitutes. That is because AM effectively tackles the dilemma between freeform design and manufacturability, enabling accurate control over implant properties through rational geometrical design. Laser power bed fusion (LPBF) has been demonstrated to be an AM approach well-suited for fabricating complex scaffolds made of biodegradable metals [11-14].

Montani et al. [15] were the first using LPBF to fabricate pure Zn potentially for biodegradable implant applications. However, partly due to the vaporization of Zn (with a normal boiling point of 907 °C) during LPBF, the fabricated Zn flat samples ($5 \times 5 \times 1$ mm^3) reached a relative density of 88 % only. Demir et al. [16] and Lietaert et al. [17] optimized the LPBF process for pure Zn and achieved relative densities exceeding 99 %. Nonetheless, the mechanical properties of LPBF pure Zn cannot match those of the human cortical bone. An effective approach to improve the mechanical properties of Zn-based biomaterials is to alloy zinc with essential trace elements in the human body, such as magnesium (Mg) [18]. Mg is not only a biodegradable metal but also a bioactive element that plays a role in bone metabolism and vascular formation [19]. Yang et al. [20] investigated the effect of Mg content (0–4 weight percent (wt%)) on the comprehensive properties of the LPBF Zn-Mg alloys with residual porosities of 1.8–2.6 % and found that the mechanical properties increased with increasing Mg content till 3 wt% Mg. The bulk Zn-3Mg alloy exhibited the highest ultimate tensile strength and elongation, along with improved biodegradation resistance and biocompatibility. The greatly enhanced mechanical properties were attributed to a combination of grain refinement, solid solution strengthening, and precipitation strengthening by the eutectics formed at grain boundaries. Qin et al. [21] and Voshage et al. [22] also studied the effects of the Mg content on the mechanical properties of Zn-*x*Mg ($x = 1, 2, 5$ wt%) alloys. However, they found that the solid Zn-1Mg specimens exhibited the highest tensile strength and tensile elongation as compared to the Zn-2Mg and Zn-5Mg specimens. Porous Zn-1Mg alloy scaffolds based on the diamond unit cells and body-centered cubic unit cells possessed the highest compressive strengths. They attributed the improved tensile strengths of Zn-1Mg, relative to those of pure Zn, to the same strengthening mechanisms as mentioned above. These inconsistent results suggest that, besides chemical composition, powder characteristics, and structural design, the LPBF processing play a major role in influencing the mechanical properties of Zn-Mg alloys. The influence of LPBF process parameters on the microstructures and properties of Zn-Mg alloys is not yet well understood. In addition, none of the above-mentioned researchers have not evaluated the compressive properties of LPBF bulk Zn-Mg alloys that could be directly compared with those of LPBF porous Zn-Mg alloys and are more relevant to bone implant applications. The compressive properties of the LPBF porous Zn-Mg structures demonstrated so far (*i.e.*, compressive strengths being $<$ 42 MPa [22]) fall short of the properties exhibited by the human cortical bone (*i.e.*, compressive yield strength of 170–193 MPa and an elastic modulus as high as 20 GPa) [23]. Ning et al. [24] carried out the compression tests of the LPBF Zn-3Mg bulk materials and found that the horizontal specimens had a yield strength of 372 MPa and a compressive strain of more than 20 %. Moreover, the Zn-3Mg alloy is a near-eutectic one and thus a large amount of the intermetallic phase is expected [25], which can significantly increase the hardness and compressive strength of the alloy [26]. This will be specifically beneficial for bone substitutes, considering the compressive stress being the main mode of loading on the bones in the body.

Here, we studied the effects of the LPBF process parameters on the microstructures and comprehensive properties of Zn-3Mg, including tensile and compressive mechanical properties, biodegradation behavior, and biological activity in comparison with pure Zn. The study was intended to pave the way for the development of functionally graded Zn-3Mg scaffolds with mechanical properties that could match those of cortical bone, thereby demonstrating the potential of the Zn-3Mg alloy as a bone-substituting material, particularly for load-bearing bone implant applications.

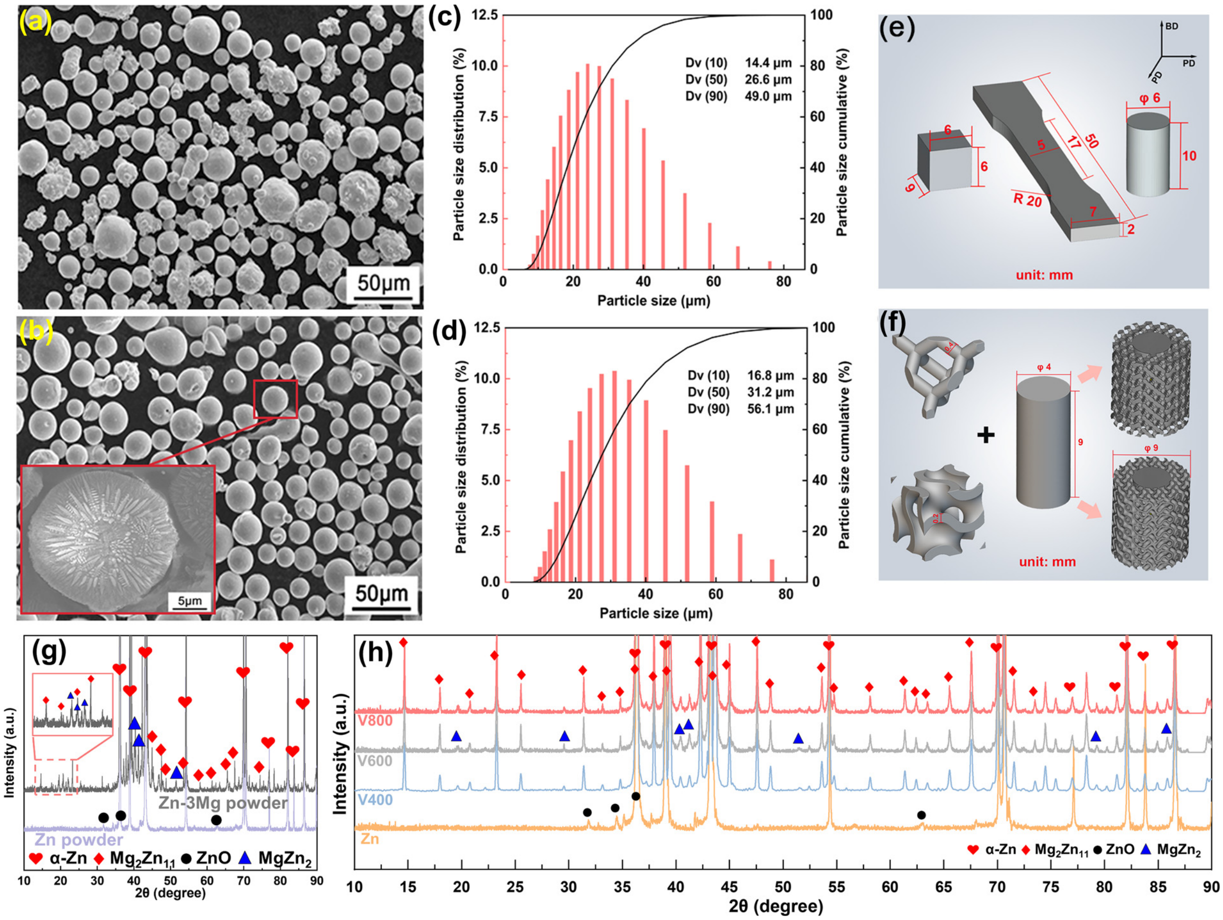

Fig. 1. The powder characteristics and schematic illustrations of the LPBF specimens: (a) Zn powder particle morphology, (b) Zn-3Mg powder particle morphology, (c) Zn powder particle size distribution, (d) Zn-3Mg powder particle size distribution, (e) the LPBF specimens and their dimensions for characterization (cubic specimens) and mechanical evaluation (flat and cylindrical specimens), (f) functionally graded specimens, (g) XRD patterns of the powders, and (h) XRD patterns of the as-built specimens.

2. Material and methods

2.1. Zn and Zn-3Mg powders

Argon-atomized Zn powder and Zn-3Mg powder with nearly spherical morphologies (Fig. 1a, b) were used for preparing the LPBF specimens. The pre-alloyed Zn-3Mg powder showed a dendritic internal structure after being polished and etched. The particle size distributions of the powders coincided with a Gaussian distribution, with D_{50} values of 26.6 μm for the Zn powder and 31.2 μm for the Zn-3Mg powder (Fig. 1c, d). The actual Mg content of the Zn-3Mg powder was 3.21 % (Table 1), determined using inductively coupled plasma (ICP) spectroscopy.

2.2. LPBF process for specimen preparation

A commercial LPBF machine (SLM 125, SLM Solution Group AG, Germany) was used for specimen preparation. The residual oxygen content in an argon gas atmosphere was controlled below 30 ppm during 3D printing. All the groups of the specimens were printed at the same layer thickness of 30 μm, hatch distance of 70 μm, beam size of 75 μm, and zig-zag scanning pattern rotated 90° at each layer. Pure Zn specimens were prepared with a laser power (*P*) of 60 W and a scanning speed (*V*) of 600 mm/s (denoted as Zn hereafter). Zn-3Mg specimens were prepared with a laser power of 70 W and different scanning speeds (V = 400 mm/s, 600 mm/s, and 800 mm/s, denoted as V400, V600, and V800, respectively, hereafter) (Table 2). Under these conditions, bulk cubic specimens, flat reduced-gage-section tensile specimens, and cylindrical compressive specimens were fabricated (Fig. 1e). Two functionally graded specimens were designed by combing the diamond or gyroid porous structure with a solid pillar (Fig. 1f). The LPBF process parameters used for the bulk and porous regions were the same, *i.e.*, at a laser power of 70 W and scanning speed of 600 mm/s.

Table 1
Chemical compositions of the Zn and Zn-3Mg alloy powders (wt%) for LPBF.

wt%	Zn	Mg	O
Zn	99.91	0	<0.1
Zn-3Mg	96.69	3.21	<0.1

2.3. Microstructural characterization

An X-ray diffractometer (XRD, TTR 3, Rigaku, Japan) was used to identify the phases in the powders and in the LPBF Zn and Zn-3Mg

Table 2
LPBF parameters for different Zn and Zn-3Mg specimen groups.

Specimen	Laser power (W)	Scanning rate (mm/s)
Zn	60	600
V400	70	400
V600	70	600
V800	70	800

specimens. Cu Kα radiation was used at a scan rate of 8°/min and over a 2θ angle range between 10° and 90°. After being ground and polished, the specimens were etched with a 5 % nitrate alcohol solution (*i.e.*, 95 ml alcohol mixed with 5 ml nitric acid). The polished surfaces and metallographic structures of the specimens were observed by using optical microscopy (OM, Olympus, Japan) and scanning electron microscopy (SEM) equipped with an energy-dispersive X-ray spectroscope (EDS) (Regulus 8100, Hitachi High-Tech, Japan). The tensile fractographs of the bulk specimens were observed by using SEM to analyze the fracture mechanism. Electron back-scattered diffraction (EBSD) was performed with an Oxford Instruments AZtec analytical system attached to SEM (JSM-7001 FEG, JEOL Ltd., Japan). The EBSD specimens were prepared by applying electrolytic polishing. The specimens were first polished using a silica suspension with a particle size of 0.05 µm for 30 min. The polished specimens were ultrasonically cleaned in absolute ethanol for 1 min, followed by drying with cold air. Then, the EBSD specimens were electrolytically polished in a solution composed of 37 vol% phosphoric acid and 63 vol% ethanol at a voltage of 3 V and at room temperature for 10 s. The specimens were obtained by washing with absolute ethanol and drying with cold air once again. The inverse pole figure (IPF) and average grain size were obtained by using the Tango application in the HKL Channel 5 software. The parameters used for grain size measurement by means of EBSD were: minimum grain boundary misorientation: 2°; number of pixels per grain: >100. The generated EBSD data were used to plot the area-weighted fraction against equivalent circle diameter to determine the mean value in 2D. The pole figure (PF) analysis was mainly carried out by the Mambo software. An FEI Titan Cube 80–300 transmission electron microscope (TEM, FEI, USA) was used at an accelerating voltage of 200 kV to observe the second phase. The selected area electron diffraction (SAED) patterns were used to characterize the crystal structure of the second phase. Prior to the TEM analysis, the specimens were ground to 50 µm, then punched into $\phi 3$ mm discs and thinned with a Gatan 695 ion thinner (Gatan, USA). Micro-computed tomography (Micro-CT, SkyScan2211, Bruker, Germany) was used to scan the two functionally graded specimens with the following parameters: 130 µA tube current, 120 kV tube voltage, and 5 µm^3 resolution.

2.4. Mechanical tests

Tensile and compressive specimens (Fig. 1e) were prepared according to the GB/T 228–2002 and GB/T 7314–2017 standards, respectively. A universal testing machine (Instron 5569, Instron, USA) was used for the tensile tests and compressive tests at the crosshead speeds of 0.1 mm/min and 1 mm/min, respectively. The tensile tests ended with the fracture of the specimens, while the compressive tests were terminated when a strain of 60 % was reached. The fracture surfaces of the tensile specimens were observed by using SEM. Three specimens in each group were tested under tensile or compressive loading.

2.5. Electrochemical tests

The electrochemical performances of the Zn and Zn-3Mg specimens in the simulated body fluid (SBF) [13] at 37 °C were studied using an electrochemical workstation (ModuLab XM, AMETEK, UK). A three-electrode electrochemical cell was set up with a Zn (or Zn-3Mg) specimen as the working electrode, a platinum plate as the counter electrode, and a saturated calomel electrode as the reference electrode. The specimen was first soaked in SBF for stabilization. The open circuit potential (OCP) was monitored for 1800s, followed by an electrochemical impedance spectroscopy (EIS) test at an amplitude of 5 mV and over a frequency range from 10^5 Hz to 10^{-2} Hz. Finally, the potentiodynamic polarization (PDP) test was conducted over a range of -100 mV to $+500$ mV *versus* OCP at a scan rate of 1 mV/s. Three specimens were prepared for each group. ZSimpWin 3.300 was used for electrochemical data analysis. The impedance data were fitted to the equivalent electrical circuits. In this context, R_s represents the solution resistance. CPE_f and R_f are the capacitance and resistance of the degradation products, respectively. CPE_{dl} and R_{ct} indicate the double layer capacitance and charge transfer resistance, respectively, which are used to describe the electrochemical interface of the electrolyte solution and the Zn substrate. Z_W represents the Warburg diffusion behavior in the low frequency region and χ^2 indicates the fitting quality.

2.6. In vitro *immersion tests*

In vitro immersion tests were carried out in the SBF [13] at 37 °C for up to 28 days with a volume to surface area ratio of 20 mL/cm^2. The corrosion products were characterized with SEM, EDS, XRD, and X-ray photoelectron spectroscopy (XPS, Kratos AXIS-Ultra DLD, Shimadzu, Japan). After removing the corrosion products with a 100 g/L ammonium chloride solution, the weight loss of the specimens was calculated. The corrosion rate was determined according to ASTM G31–72[27]:

$$CR_w = \frac{K \times W}{A \times T \times D} \tag{1}$$

where CR_w is the corrosion rate (mm/year), K is a dimensionless constant (8.76×10^4), W is the weight loss (g), A is the area of the specimen exposed to SBF (cm^2), T is the immersion time (h), and D is the density of the material (g/cm^3). All the tests were performed in triplicate. The concentrations of Zn^{2+}in SBF were measured using an inductively coupled plasma optical emission spectroscope (ICP-OES, OPTIMA 7000 DV, PerkinElmer, USA) at different time points.

2.7. Cytocompatibility tests

A murine calvaria-derived osteoblast cell line (MC3T3-E1, ATCC–CRL-2594) was utilized for cytocompatibility tests. The Zn and Zn-3Mg specimens were incubated in a cell culture medium (*i.e.*, alpha minimal essential medium (α-MEM) containing 10 % fetal bovine serum and 1 % double antibody) at 37 °C and in a 5 % CO_2 atmosphere for 3 days to obtain the corresponding extracts. The ratio of the medium volume to the surface area of the specimen was 1.25 mL/cm^2. The extracts were diluted into 20 % and 10 % concentrations for subsequent cell culturing. The negative control was α-MEM while the positive control consisted of α-MEM supplemented with 10 % dimethyl sulfoxide (DMSO, Invitrogen, USA). After 1 and 3 days of culture, the extracts (or the control media) were replaced with fresh medium and cellular activities were determined by using the CCK-8 cell counting kit (Dojindo Molecular Technology, Japan). Cell staining was performed with the Calcein-AM/PI Live/Dead Cell Double Staining Kit (Solarbio, China) under protection from light.

To assess the bone regeneration ability, the MC3T3-E1 cells were co-cultured with the 10 % and 20 % diluted extracts in subsequent tests. Alkaline phosphatase (ALP) staining and quantitative assessments of the cells cultured up to 14 and 21 days, with the medium changed every 2 days, were conducted. At 14 and 21 days, the medium was removed and the cells were gently rinsed with the phosphate buffered saline (PBS) buffer solution 3 times. After fixing with formaldehyde, the cells were gently rinsed with the PBS buffer 3 times once again. ALP staining was conducted with the 5–bromo-4–chloro-3-indolyl phosphate (BCIP)/nitro blue tetrazolium (NBT) alkaline phosphatase color development kit (Beyotime Biotechnology, China). Protein extraction from the cells was carried out using the RIPA Lysis Buffer (Hangzhou Fude Biological Technology, China). The ALP activity of the MC3T3-E1 cells was quantitatively determined using an ALP/AKP assay kit (Nanjing Jiancheng Institute of Biology, China). α-MEM was used as the control.

For Alizarin Red (AR) staining and quantitative analysis, the cells were cultured until 21 days, which was the same as for the ALP assay. Then, the medium was removed and the cells were gently rinsed with the PBS buffer 3 times. After fixating the cells with formaldehyde, the cells were gently rinsed with the PBS buffer 3 times once again. AR staining was performed using the osteoblast mineralization nodules staining kit (Beyotime Biotechnology, China). After staining, 1 mL of pure water was added to each well and the wells were placed in a refrigerator at 4 °C for 7 days to remove any remaining AR dye solution. Subsequently, the pure water in each well was removed and 10 % cetylpyridine was added for quantitative analysis. α-MEM was used as the control. More than three samples were tested from each group.

2.8. Statistical analysis

Statistical analysis of the biocompatibility results was performed using a two-way ANOVA test with a *post-hoc* Tukey's multiple comparison test. A significance level of α=0.05 was used for all the analyses (* represents $p < 0.05$; ** represents $p < 0.01$).

3. Results

3.1. Microstructures

Under OM, the longitudinal sections (*i.e.*, sections along the building direction (BD)) of the polished LPBF Zn and Zn-3Mg specimens showed no evident defects or cracks formed under different LPBF process conditions (Fig. 2a-d), save for a few micro-scale pores. The relative densities of the AM specimens were 99.53±0.22 %, 99.44±0.13 %, 99.82±0.17 %, and 99.71±0.1 %

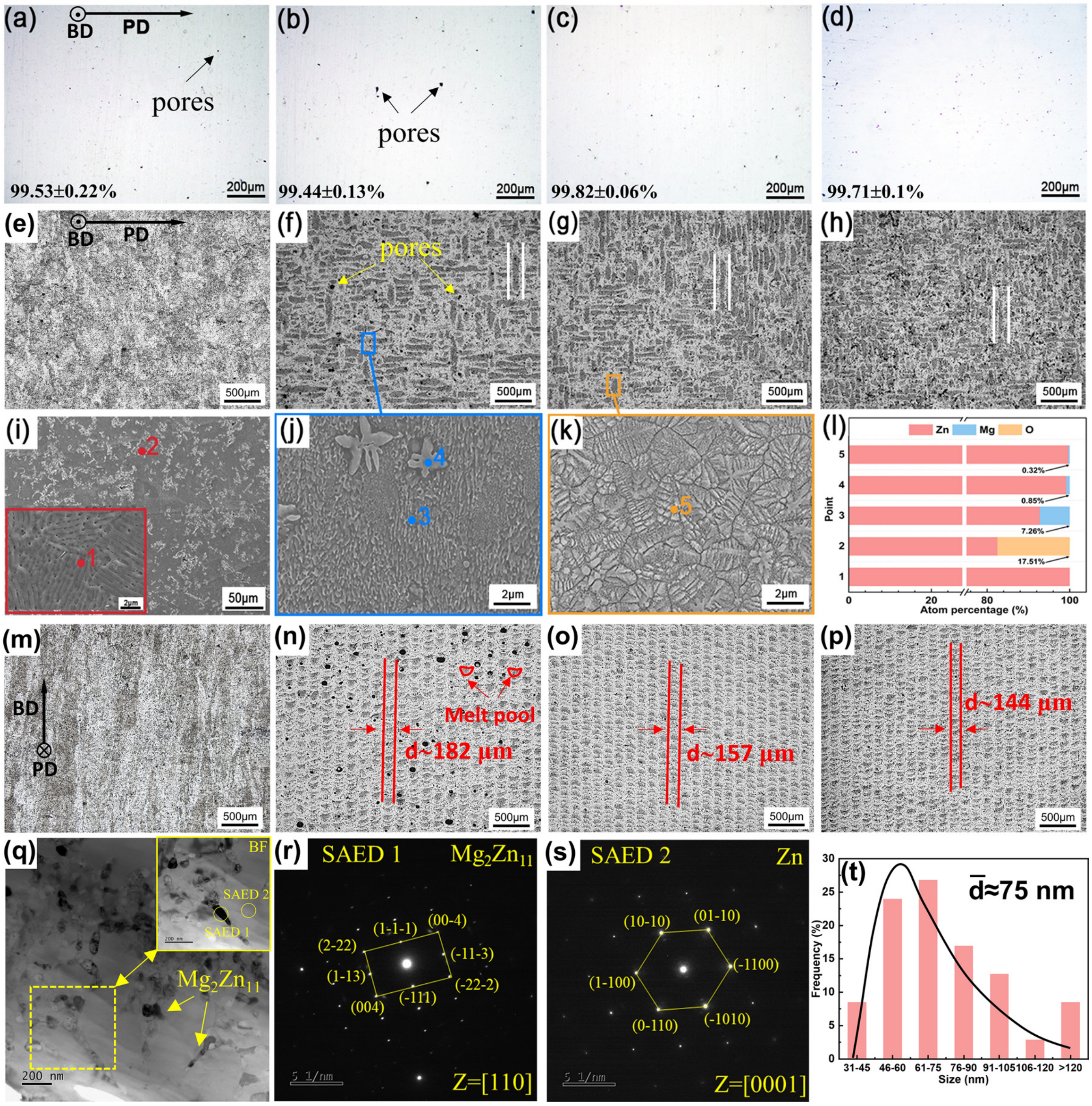

Fig. 2. Microstructure analysis of the LPBF specimens: (a-d) polished and (e-h) etched surfaces of the as-built Zn, V400, V600, and V800 specimens in the printing direction (PD) (the white lines indicate the melt pool width), (i) SEM images of the LPBF Zn specimens, (j-k) SEM images of the LPBF Zn-3Mg alloy specimens printed at scanning speeds of 400 and 600 mm/s, respectively, (l) the results of EDS point analysis at various spots (i-k), (m-p) etched surfaces of the as-built Zn, V400, V600, and V800 specimens in the building direction (BD) (the red lines indicate the melt pool width), (q) TEM bright-field image of the as-built V600 specimen, (r-s) the Zn matrix and second phase SAED patterns in (q), and (t) the size distribution of Mg_2Zn_{11} in the V600 specimen shown in (q).

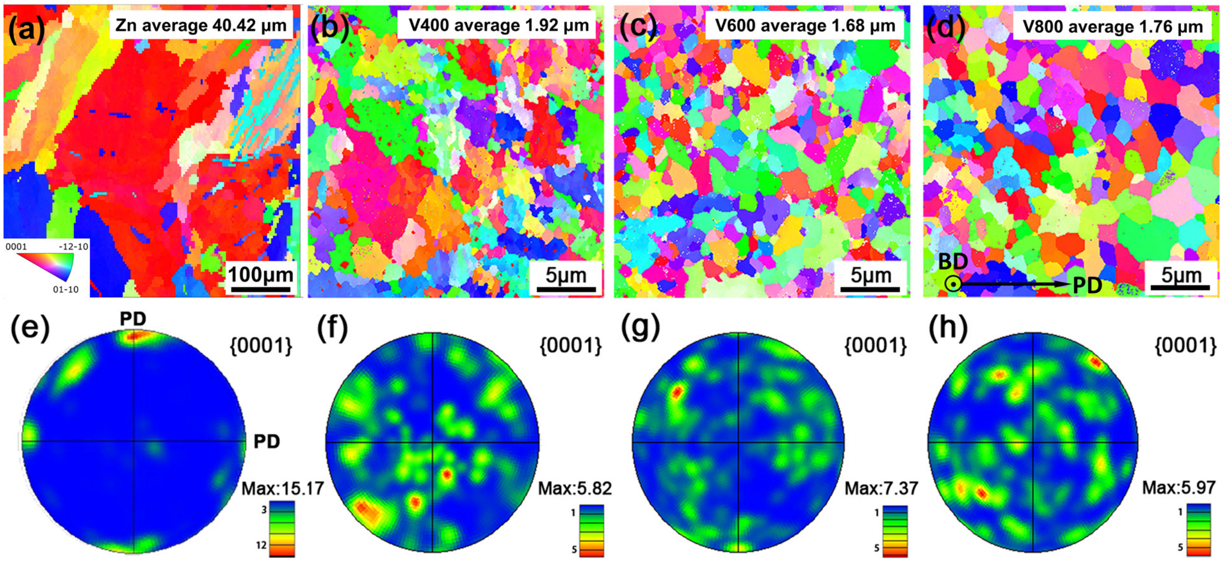

Fig. 3. EBSD analysis of the LPBF specimens: (a-d) inverse pole figure maps visualizing the morphologies and grain sizes in the printing direction (PD), (e-h) {0001} pole figures showing texture intensities: (a, e) Zn, (b, f) V400, (c, g) V600, and (d, h) V800.

for the Zn, V600, V700, and V800 specimens, respectively. After etching, an interlaced white and grey morphology appeared on the Zn-3Mg specimens (Fig. 2f-h), which was different from the microstructure of the as-built pure Zn (Fig. 2e) and indicated that a dual-phase microstructure was present in the Zn-3Mg specimens.

The width of the melt pool decreased with the scanning speed (Fig. 2f-h). Further examination using SEM at a higher magnification and EDS analysis indicated that the microstructure was composed of the white region, consisting of the α-Zn and Mg_2Zn_{11} eutectic phases along with a small amount of the primary α-Zn dendrite phase (Fig. 2j, l) while the grey region was the α-Zn dendrite phase (Fig. 2k, l). For pure Zn, however, SEM images showed cellular grains and irregular white particles containing a larger amount of oxygen (*e.g.*, point 2 in Fig. 2i and l), as compared to the matrix (point 1 in Fig. 2i and l). The XRD analysis revealed the presence of the ZnO phase (Fig. 1g) both in the pure Zn powder and in the LPBF pure Zn specimens. While the α-Zn, ZnO, Mg_2Zn_{11}, and $MgZn_2$ phases could be detected in the Zn-3Mg powder, in the LPBF Zn-3Mg alloy (Fig. 1h) the peaks of the ZnO and $MgZn_2$ phases were not obvious.

EBSD inverse pole figure (IPF) map analysis revealed that the LPBF Zn had larger, irregular grains (Fig. 3a), whereas the LPBF Zn-3Mg alloy largely consisted of smaller equiaxed ones (Fig. 3b-d). The grain sizes of the pure Zn were mostly within a range smaller than 10 μm, with a mean value of 40.42 μm (Fig. 3a). In contrast, the grain sizes of the Zn-3Mg alloy were much smaller with mean values around 1 μm (Fig. 3a-d). When the laser scanning speed increased from 400 mm/s to 600 mm/s and 800 mm/s, the mean grain size of the Zn-3Mg specimens slightly decreased from 1.92 μm to 1.76 μm and 1.68 μm. According to the pole figure (PF) analysis (Fig. 3e-h), the grains of the pure Zn and Zn-3Mg alloy had no obvious preferred orientation in the printing direction, similar to the building direction (Figure S1). Zn-3Mg generally displayed reduced texture intensities as compared to pure Zn, with V600 having a greater texture intensity value than V400 and V800 (Fig. 3f-h). Bright-field images (Fig. 2q) and SAED analysis (Fig. 2r, s) confirmed the presence of the Mg_2Zn_{11} phase in the LPBF Zn-3Mg specimens. The mean size of Mg_2Zn_{11} phase particles was about 75 nm (Fig. 2t).

3.2. Mechanical properties

The tensile tests showed that the addition of 3 wt% Mg to Zn greatly increased the ultimate tensile strength (UTS) but decreased the elongation of the LPBF Zn specimens (Fig. 4a, b). Among the specimens produced at different scanning speeds, V600 exhibited the highest UTS and ductility. Based on the patterns observed on the fractographic images (Fig. 4e-h), the pure Zn specimens had a mixture of ductile and brittle fracture features, characterized by both large-area cleavage planes and numerous dimples (Fig. 4e). In contrast, the Zn-3Mg alloy exhibited a clear brittle fracture surface composed of many cleavage planes (Fig. 4f-h).

The compressive mechanical properties of both Zn and Zn-3Mg were superior to (Fig. 4c, d) their tensile properties (Fig. 4a, b). The highest compressive yield strength (YS) of Zn-3Mg reached 601.12±16.45 MPa, which was 6 times as high as that of pure Zn. There were no significant differences in compressive YS and ultimate compressive strength (UCS) between the V400, V600, and V800 specimens. Moreover, all the specimens could be compressed to a pre-determined strain of 60 % without breakage.

3.3. Electrochemical behavior

Based on the Bode plots of the Zn and Zn-3Mg specimens (Fig. 5a), at low frequencies, the impedance modulus $|Z|$ followed the descending order: V400, V800, V600, and Zn. For both materials, the phase angles at high frequencies were larger than those at low frequencies (Fig. 5b). The Nyquist curves of all the specimens were composed of a semicircle in the high-frequency region and a straight line in the low-frequency region (Fig. 5c). The diameters of the semicircles, D, followed the trend: $D_{\mathrm{V400}} > D_{\mathrm{V800}} > D_{\mathrm{V600}} > D_{\mathrm{Zn}}$. The fitted equivalent circuit revealed that R_f of Zn was larger than the R_f values of V600 and V800, but lower than that of V400 while the R_{ct} values of all the Zn-3Mg specimens were larger than R_{ct} value of the pure Zn specimens (Table 3).

From the PDP analysis, both the Zn and Zn-3Mg alloy specimens exhibited similar patterns of polarization where passivation occurred in the anode region when the anode potential was high enough to stabilize the oxide film (Fig. 5d). All the Tafel curves

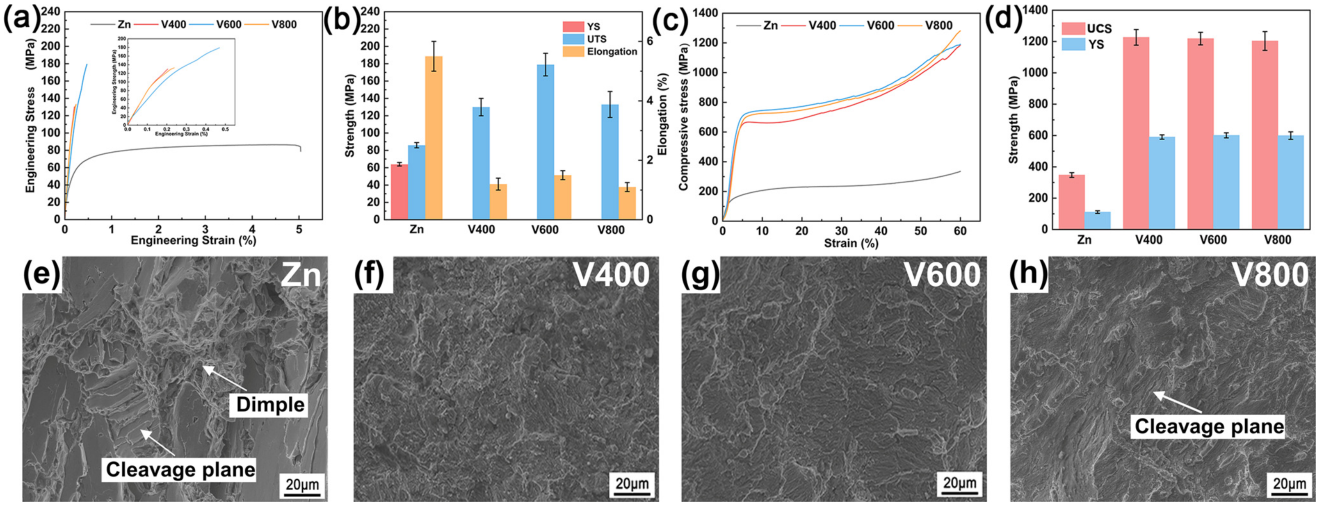

Fig. 4. Mechanical properties: (a) tensile stress-strain curves, (b) tensile properties, (c) compressive stress-strain curves, (d) compressive properties, and (e-h) tensile fractographs of the Zn, V400, V600, and V800 specimens.

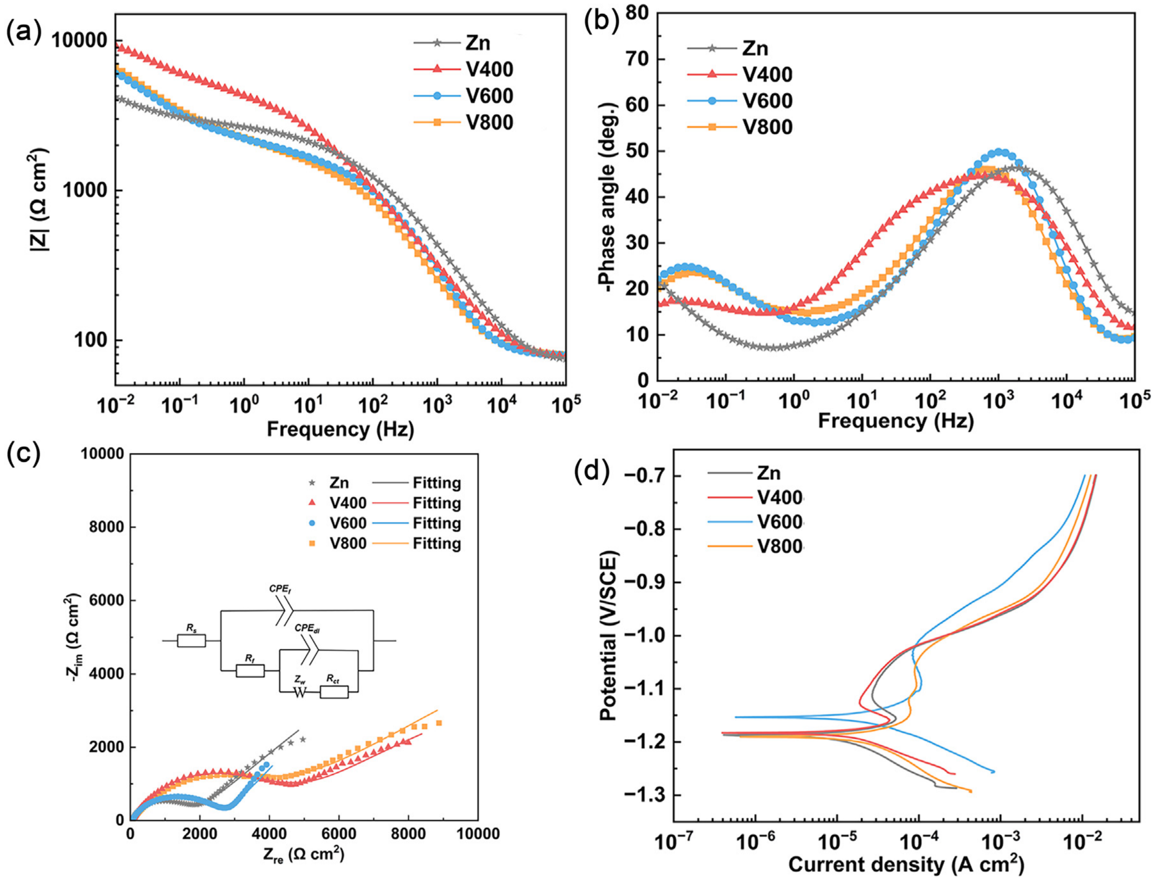

Fig. 5. Electrochemical behavior: (a) Bode plots of impedance modulus |Z| against frequency, (b) Bode plots of phase angle against frequency, (c) Nyquist plots and equivalent circuit, and (d) potentiodynamic polarization curves.

were characterized by a sudden drop after the breakdown potential. The breakdown potential values of the V600 and V800 specimens were higher than those of the V400 and Zn specimens. It was observed that, with 3 wt% Mg added to Zn, the corrosion potential did not change significantly (Table 4). However, the corrosion current density (i_{corr}) was notably decreased from 16.12±1.28 μA/cm^2. Among the Zn-3Mg specimens, V600 had the highest i_{corr} value (13.99±0.65 μA/cm^2) as compared to V400 (7.64±0.35 μA/cm^2) and V800 (11.07±0.48 μA/cm^2).

3.4. In vitro *degradation behavior*

During *in vitro* immersion, white degradation products gradually formed on the surfaces of the LPBF Zn and Zn-3Mg specimens from day 1 to day 28 (Fig. 6a). EDS analysis showed that the biodegradation products on the pure Zn specimens mainly contained Zn, Ca, P, C, and O, while the biodegradation products on the Zn-3Mg specimens were mainly composed of Zn, Mg, Ca, P, C, and O (Fig. 6b). After 28 days of immersion, the Ca, P, and O contents of

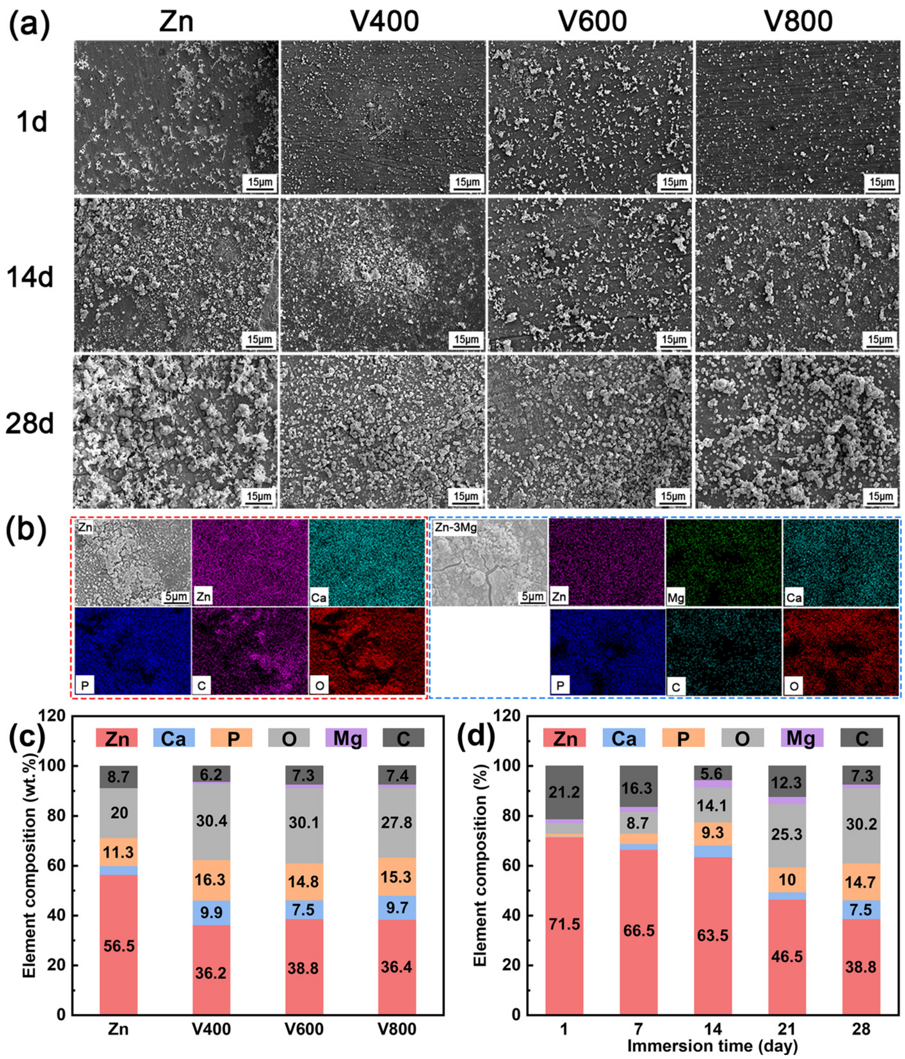

Fig. 6. Characteristics of the corrosion products: (a) morphologies of the corrosion products on the specimens at different immersion time points, (b) EDS mapping of the corrosion products on Zn and Zn-3Mg, showing elemental distributions, (c) the compositions of the corrosion products on different specimens after 28 days of immersion, and (d) the compositions of the corrosion products on the V600 specimens at different immersion time points.

the biodegradation products of the Zn-3Mg specimens were higher than those of Zn (Fig. 6c). The V600 specimens had lower Ca and P contents as compared to V400 and V800. Furthermore, the Ca, P, and O contents of the biodegradation products of V600 increased with the immersion time (Fig. 6d).

XRD analysis showed that the biodegradation products on Zn were mainly ZnO, while the biodegradation products on Zn-3Mg were composed of $Zn(OH)_2$, $Zn_5(OH)_6(CO_3)_2$, and a small amount of Na_2CO_3 (Fig. 7a, b). Similarly, the full spectra of XPS showed that the biodegradation products on all the specimens were mainly composed of Zn, Ca, P, C, and O (Fig. 7c). High-resolution spectra of the Zn-2$p_{3/2}$ peaks were collected and fitted for different specimens after 28 days of *in intro* immersion (Fig. 7g). The 1021 eV, 1020 eV, and 1019 eV signals may be attributed to $Zn_5(OH)_6(CO_3)_2$, $Zn(OH)_2$, and ZnO, respectively.

From the ICP analysis, it was clear that the ion release rate from Zn was lower than that from Zn-3Mg during the first 14 days. However, from day 14 to day 28, the biodegradation rate of Zn rapidly increased and then exceeded that of Zn-3Mg (Fig. 7d). Based on the results from weight loss tests, Zn was found to degrade at higher rates than Zn-3Mg at all immersion time points (Fig. 7e, F). The biodegradation rate of Zn reached 0.20 ± 0.01 mm/year at day 28. Among the three Zn-3Mg specimens, V600 had the highest degradation rate at day 28, which was 0.15 ± 0.01 mm/year.

3.5. In vitro *cytocompatibility*

From the CCK-8 tests, cell viability was found to decrease with the extract concentration (Fig. 8a-b). In general, cell viability improved with the culture time. The V600 specimens exhibited the best cell viability at different extract concentrations, reaching 116±8 % with 0-grade cytotoxicity when the extracts were diluted to 10 % (Fig. 8a). The ionic concentrations of the 100 % extracts from the Zn and Zn-3Mg specimens were measured (Fig. 8c). Zn^{2+} release from Zn was less than that from Zn-3Mg, which was consistent with the results obtained from the *in vitro* immersion tests at day 3 (Fig. 7d). The V600 specimens released more $Zn^{2+}$and Mg^{2+} as compared to the V400 and V800 specimens.

Live/dead staining showed that for both materials, most of the cells were alive (green) with the 10 %-diluted extracts having higher densities of viable cells than the 20 %-diluted extracts. The number of viable cells was comparable to the negative control (α-MEM) and significantly higher than the positive control (DMSO). The MC3T3 cells cultured with the Zn and Zn-3Mg extracts showed

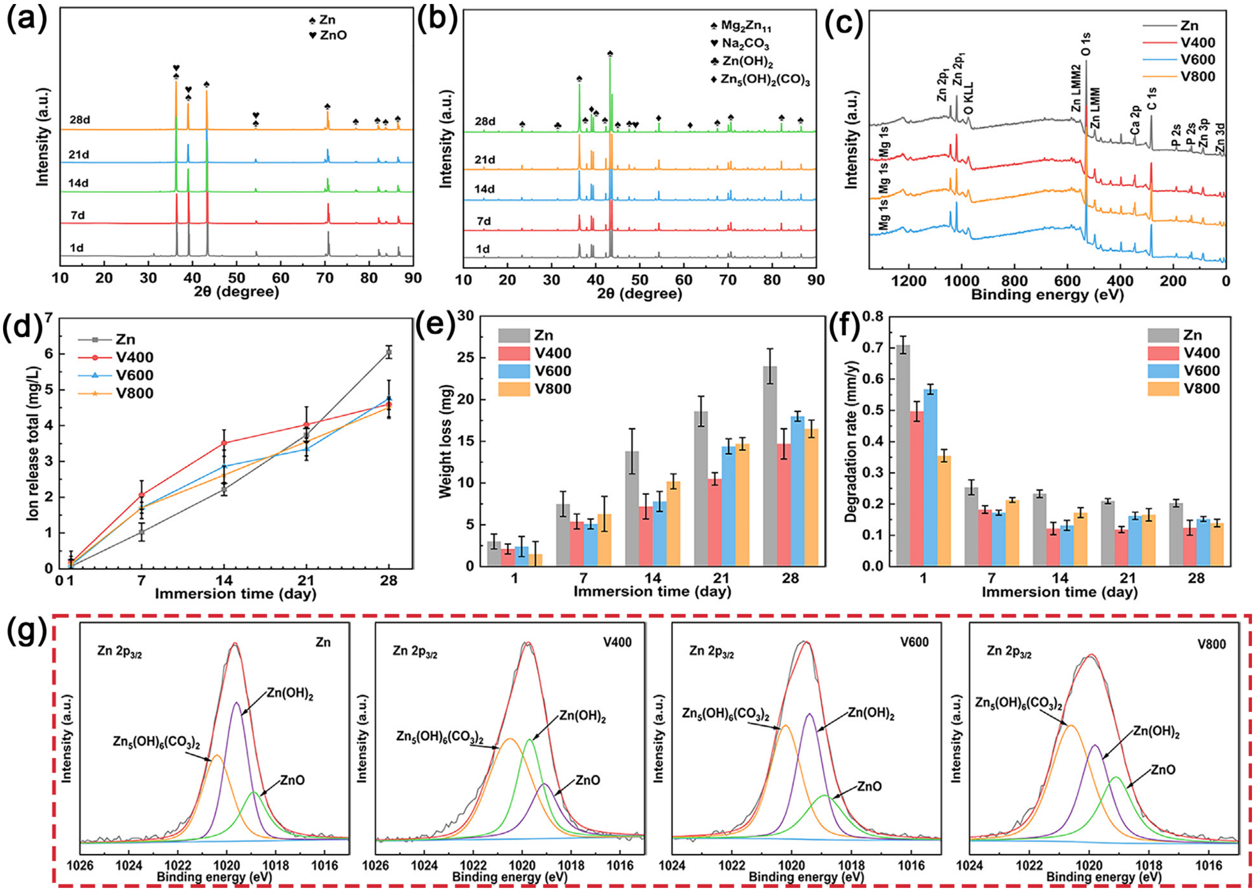

Fig. 7. Results of the *in vitro* biodegradation tests and analyses of the biodegradation products: (a) XRD patterns showing the phase evolutions of the LPBF Zn specimens over immersion time, (b) XRD patterns showing the phase evolutions of the LPBF Zn-3Mg specimens with immersion time, (c) the XPS full spectra of the corrosion products on different specimens after 28 days of immersion in the SBF, (d) the variations of Zn^{2+} release from the LPBF specimens with the immersion time, (g) the weight losses of the LPBF specimens at different immersion time points, (f) the biodegradation rates of the LPBF specimens at different immersion time points, and (g) high-resolution spectra of the Zn $2p_{3/2}$ peaks collected from the biodegradation products on the LPBF specimens after 28 days of immersion in the SBF.

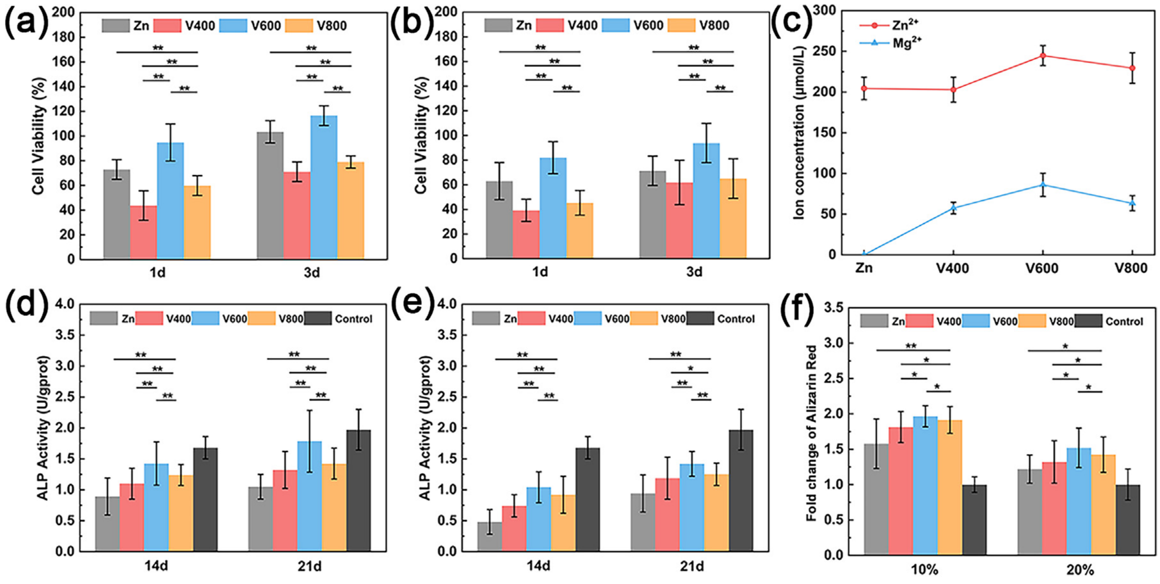

Fig. 8. *In vitro* quantitative cytocompatibility assessments: (a, b) the viability of MC3T3 cells cultured with the 10 %- and 20 %-diluted extracts for 1 and 3 days, respectively, (c) Zn^{2+} and Mg^{2+}concentrations in the 100 % extracts, (d, e) ALP activities of the MC3T3 cells cultured with the 10 %- and 20 %-diluted extracts for 14 and 21 days, respectively, and (f) the fold changes of Alizarin Red with the 10 %- and 20 %-diluted extracts for 21 days in comparison with the control.

Table 3
EIS fitting parameters of the Zn and Zn-3Mg specimens.

Specimen	Rs ($\Omega\cdot cm^2$)	CPEf (10^{-6} $\Omega^{-1}\cdot s^n\cdot cm^{-2}$)	n1	Rf ($k\Omega\cdot cm^2$)	CPEdl (10^{-4} $\Omega^{-1}\cdot s^n\cdot cm^{-2}$)	n2	Rct ($k\Omega\cdot cm^2$)	Zw (10^{-3} $\Omega^{-0.5}\cdot s^{-1}\cdot cm^{-2}$)	$\chi 2$ (10^{-4})
Zn	63.39±5.21	3.74±0.35	0.73±0.09	1.42±0.11	0.38±0.08	0.60±0.12	1.18±0.23	1.89±0.18	3.19±0.27
V400	65.20±2.24	12.41±0.74	0.65±0.04	2.59±0.12	2.18±0.11	0.25±0.03	8.97±1.12	0.18±0.03	9.18±0.85
V600	76.03±12.78	1.86±0.75	0.85±0.02	0.18±0.03	1.21±0.20	0.24±0.05	2.58±0.23	0.52±0.05	5.93±1.21
V800	72.90±8.35	6.00±2.65	0.71±0.09	0.04±0.01	1.06±0.23	0.12±0.03	8.48±0.26	0.26±0.09	5.22±0.42

Table 4
Results obtained from potentiodynamic polarization tests and corrosion rates obtained by applying the weight loss method.

Specimen	E_{corr} (V/SCE)	i_{corr} ($\mu A/cm^2$)	CR_i (mm/year)	CR_w (mm/year)
Zn	−1.19±0.02	16.12±1.28	0.52±0.01	0.20±0.01
V400	−1.18±0.02	7.64±0.35	0.26±0.01	0.12±0.02
V600	−1.16±0.01	13.99±0.65	0.48±0.01	0.15±0.01
V800	−1.19±0.03	11.07±0.48	0.38±0.02	0.13±0.01

far-stretching filopodia-like protrusions, which was similar to the negative control (α-MEM) (Fig. 9a).

The ALP activity of the cells cultured with the Zn-3Mg extracts were higher than those with the pure Zn extracts (Fig. 8d, e). The V600 extracts had higher ALP activity values than the V400 and V800 extracts. Generally, the ALP activity of the cells in the 10 %-diluted solution was higher than that of the 20 %-diluted solution. The ALP staining showed a darker color for the 10 %-diluted extracts as compared to the 20 %-diluted ones. The staining was more pronounced from day 14 to day 21 for both materials, although no notable differences could be observed between the different groups (Fig. 9b).

The trends of AR absorbance for the different specimens were similar to those of the ALP activity. The Zn-3Mg specimens had higher AR absorbance values than the pure Zn specimens, with V600 showing the highest absorbance value. All the specimens showed better results than the α-MEM control group (Fig. 8f). According to the AR staining results, the Zn-3Mg specimens displayed more obvious mineralized noduli than the Zn specimens, and the staining of the 20 %-diluted extracts was darker than the 10 %-diluted extracts (Fig. 9c).

3.6. Characteristics of the functionally graded structures

According to the micro-CT analysis, the macro porosity values of the gyroid and diamond functionally graded specimens were 58.6 % and 56.9 %, respectively (Fig. 10a, b). The micro porosity values of the struts and pillars of the diamond and gyroid specimens were 0.04 % and 0.06 %, respectively (Fig. 10a, b).

The compressive yield strength of the gyroid-based specimens (170.75 ± 6.43 MPa) was greater than that of the diamond-based specimens (129.34 ± 8.21 MPa) (Fig. 10g). The gyroid-based specimens showed a compressive strain of about 22 %, while the diamond-based specimens displayed smooth stress-strain curves even when the compressive strain was as high as 60 %.

The EBSD analysis of the specimens with diamond unit cells revealed more columnar grains in the building direction (BD), as compared to the grains in the printing direction (PD) (Fig. 10d). According to the pole figure (PF) analysis, both in the printing direction (PD) (Fig. 10e) and in the building direction (BD) (Fig. 10e), the grains did not have obvious preferred orientation.

During the *in vitro* immersion tests, the ion release rates from the gyroid-based specimens were lower than those from the diamond-based specimens from day 6 to day 14 (Fig. 10h). Weight loss tests showed that the gyroid-based specimens had a lower degradation rate than the diamond-based specimens at day 14 (Fig. 10i). The biodegradation rates of the diamond-based specimens and gyroid-based specimens reached 0.13 ± 0.02 mm/year and 0.1 ± 0.02 mm/year, respectively (Fig. 10i).

According to the CCK-8 tests of diamond-based specimens, the cell viability of the 10 %-diluted extracts was higher than that of the 20 %-diluted extract at day 1, while the specimens of the 20 %-diluted extracts exhibited better cell viability at day 3, reaching 108±4 % with 0-grade cytotoxicity (Fig. 10j). Live/dead staining showed that most of the cells were alive (green) with the 10 %-diluted extracts having higher densities of viable cells than the

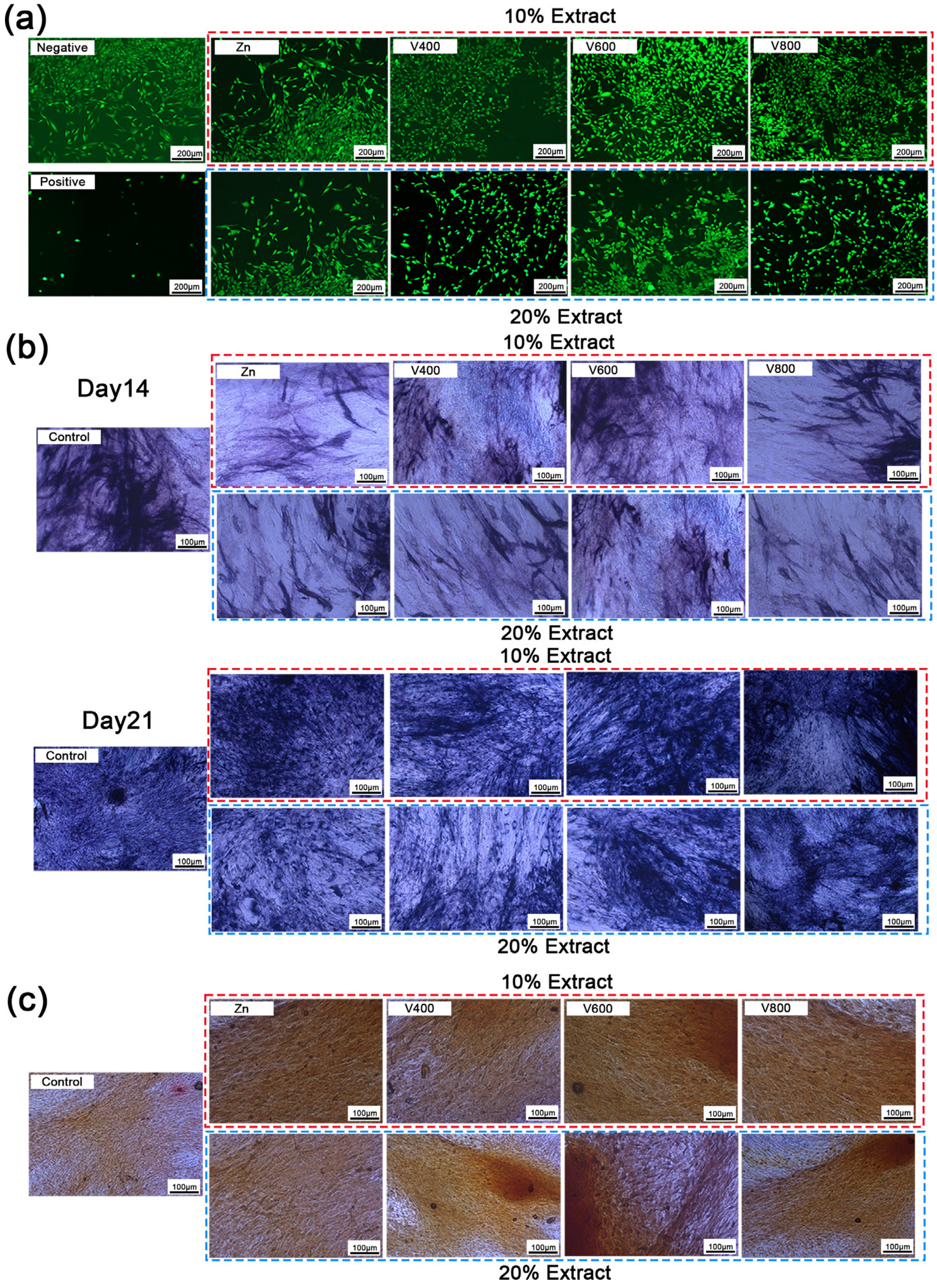

Fig. 9. *In vitro* qualitative cytocompatibility assessments: (a) live/dead staining results in the 10 %- and 20 %-diluted extracts from the different specimens for 1 day, (b) ALP staining of the MC3T3 cells cultured with the 10 %- and 20 %-diluted extracts from the different specimens for 14 and 21 days, and (c) AR staining of the MC3T3 cells cultured with the 10 %- and 20 %-diluted extracts from the different specimens for 21 days.

20 %-diluted extracts at day 1. The number of viable cells was comparable to the negative control (α-MEM) and significantly larger than the positive control (DMSO) (Fig. 10k-n).

4. Discussion

4.1. Microstructure and phase constituents

The relative densities of the LBPF pure Zn and Zn-3Mg specimens were all higher than 99 %, thereby limiting or even eliminating the effects of typical defects introduced during LPBF, such as porosity and lack-of-fusion, on how the alloying and LPBF process would affect the resultant properties. The microstructures of the LPBF Zn and Zn-3Mg specimens were clearly different from those of the cast ones. The as-cast pure Zn typically has coarse α-Zn grains, while the as-cast Zn-3Mg alloy is composed of large α-Zn dendrites dispersed in the eutectic phase (α-Zn + Mg_2Zn_{11}) structure [25]. That is due to the fact that, in this alloy, the Mg content exceeds the solubility limit (0.15 wt%) [28], leading to the formation of eutectic phases at 364 °C. The LPBF Zn and Zn-3Mg spec-

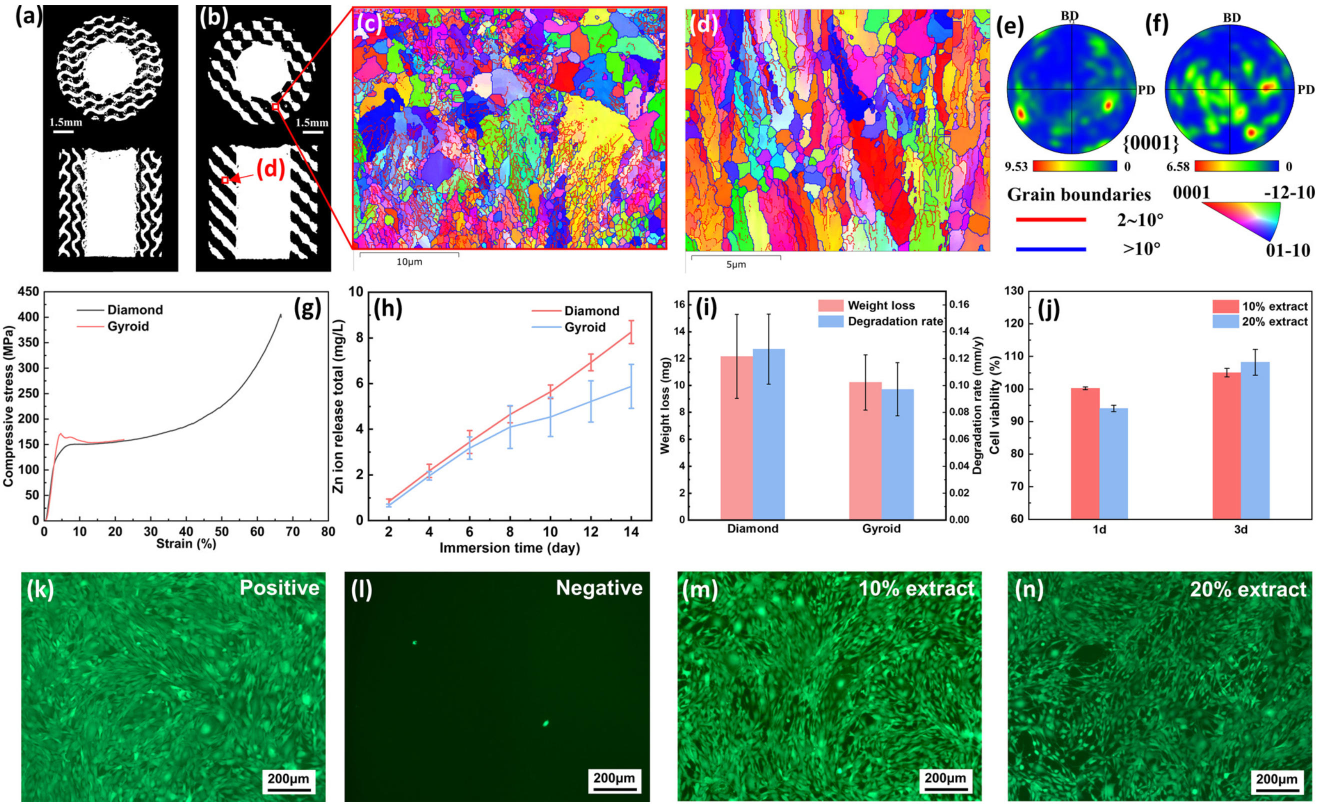

Fig. 10. Characteristics of the LPBF functionally graded Zn-3Mg scaffolds: (a, b) the micro-CT analysis of the gyroid and diamond functionally graded specimens, respectively, (c, d) inverse pole figure maps in the printing direction (PD) and in the building direction (BD), respectively, (e, f) {0001} pole figures showing texture intensities, corresponding to (c, d), respectively, (g) compressive stress-strain curves, (h) Zn^{2+} release from the LPBF functionally graded Zn-3Mg scaffolds *in vitro*, (i) the weight losses and biodegradation rates of the functionally graded Zn-3Mg scaffolds at day 14, (j) the viability of MC3T3 cells cultured with the 10 %- and 20 %-diluted extracts for 1 and 3 days, and (k-n) live/dead staining results of MC3T3 cells cultured in the 10 %- and 20 %-diluted extracts from the diamond functionally graded specimens for 1 day.

imens had significantly refined grain sizes, owing to high cooling rates (up to 10^6–10^8 K/s) involved in the LPBF process [29]. Moreover, the grain sizes of the LPBF Zn-3Mg alloy were clearly smaller than those of the LPBF Zn specimens. The rapid formation of the eutectic phases could effectively prevent the growth of the primary dendritic α-Zn phase, thus resulting in refined grains [30]. According to the binary phase diagram, the present Zn-3Mg alloy composition is situated close to the eutectic point (*i.e.*, 3.05 wt% Mg) where the eutectic temperature (364 °C) is lower than the melting point of pure Zn (420 °C) [22]. Since LPBF is a non-equilibrium rapid solidification process, the eutectic point may shift from the equilibrium value and Mg segregation may occur from the center of the melt pool to the boundaries. In the as-built microstructures of the LPBF Zn-3Mg specimens, we found α-Zn dendrites, but not the Mg_2Zn_{11} phase from the hypereutectic reaction, suggesting that the hypoeutectic reaction dominated during the solidification stage. Most likely, during the LPBF process, the fine α-Zn phase first forms in the melt pool where the Mg concentration is lower than the eutectic composition, allowing the primary dendrites to form. At the edge of the melt pool, the heat-affected zone exists since the melting of the upper layer has a thermal effect on the lower layer. Meanwhile, Mg may segregate at the boundaries of the melt pool, resulting in the formation of the eutectic phase mixtures around the α-Zn phase (Fig. 2j). With the same laser power but increasing scanning speed, the solidification speed in the melt pool increases. Therefore, the grain sizes of the specimens were found to decrease slightly when the scanning speed increased from 400 mm/s to 800 mm/s.

The grain morphology of a LPBF metal is mainly determined by the temperature gradient and solidification rate [31]. Grains prefer to grow along the LPBF building direction that has the largest temperature gradient, resulting in the formation of a columnar morphology [32]. The columnar grains grow continually by shifting their direction of epitaxial growth to align with the temperature gradient [33] along the building direction during the multiple melting-solidification processes of LPBF. Therefore, the equiaxed grain on the printing plane can be viewed on the cross-section of the columnar grains growing along the building direction (BD). In line with previous findings [22], the orientation of the grains in the LPBF Zn and Zn-3Mg specimens on the {0001} plane was relatively random with no preferred orientation. The LPBF Zn-3Mg alloy had weaker texture intensities than the LPBF Zn, which may be attributed to the transition from columnar grains toward equiaxed grains because of alloying [34] and the resultant constitutional undercooling ahead of the solid-liquid interface. The texture of LPBF metals depends on the evolution of the grain structure and is affected by the shape and sizes of melt pool and, in turn, by the LPBF process parameters, including the scanning speed [33]. This explains the small differences in the {0001} surface texture intensity between the Zn-3Mg specimens printed at various scanning speeds.

4.2. Mechanical properties

Alloying Zn with Mg greatly increased the UTS and decreased the tensile ductility of the LPBF Zn specimens, which is consistent with the results obtained by other researchers [35,36]. The increases in the tensile strengths of Zn-3Mg can be chiefly attributed to grain refinement and the presence of the second phase Mg_2Zn_{11}. Mg_2Zn_{11} is a hard but brittle phase that can decrease the tensile ductility of the Zn-3Mg alloy. In addition, according to the EBSD results, the crystal structure of Zn-3Mg is mainly hexagonal closepacked (HCP). As compared with the body-centered cubic (BCC) and face-centered cubic (FCC) structures, the number of slip systems operating in HCP crystals at room temperature is significantly smaller, which further reduces the tensile ductility of Zn and its alloys [37]. We found that tuning the LPBF process parameters could alter the mechanical properties of the Zn-3Mg alloy, especially the tensile properties (Fig. 4). V600 possessed a higher tensile strength than V400 and V800, which could be attributed to increased texture intensity (Fig. 3). However, the tensile strengths of these specimens were all low, mainly because of the low ductility of the alloy that resulted in premature failure (Fig. 4a) under tensile loading due to the presence of the brittle Mg_2Zn_{11} phase.

Since bone scaffolds are mostly subjected to compressive loading in the human body, we further investigated the compressive mechanical properties of the LPBF Zn-3Mg specimens. The compressive properties of the LPBF Zn-3Mg alloy were found to be outstanding, with yield strengths as high as 601 MPa and a strain of >60 % without failure. In previous studies, extruded Zn was found to have a peculiar tension-compression yield asymmetry (being distinctly different from other HCP-structured metals, such as extruded Mg and its alloys) due to a higher $\{10\bar{1}2\}<\bar{1}011>$ twinning activity under tension, which lowers the tensile yield strength [38]. The unusual high deformability of the LPBF Zn-3Mg alloy under compression could be attributed to the formation of compressive twin crystals during compressive deformation, as found in the Zn-1Mg alloy [39]. Furthermore, LPBF led to the formation of the Mg_2Zn_{11} phase with significantly reduced sizes and increased number density, accompanied by reduced aspect ratios. The dispersion of these fine precipitates can impede the movement of dislocations without causing large stress concentrations during deformation, leading to enhanced precipitation strengthening and ability to accommodate plastic deformation [40]. Moreover, unlike the cracks subjected to tensile stresses, the cracks under compression are difficult to grow and tend to become closed so that the material could continue to deform plastically [41].

The improvement in the yield strength can be explained according to the equation below [42]:

$$\sigma_y = \sigma_{ss} + \sigma_g + \sigma_s + \sigma_d \tag{2}$$

in which σ_y is the yield strength, while σ_{ss}, σ_g, σ_S, and σ_d are the contributions of solid solution strengthening, grain refinement strengthening, second phase strengthening, and dislocation strengthening, respectively. Due to the low solid solubility of Mg in Zn (*i.e.*, 1 wt.% at the eutectic temperature and almost zero at ambient temperature [43]), the contribution of solid solution strengthening may be negligible, as found from the EDS analysis (Fig. 2l), which deviates from the observations made by other researchers [20-22]. The grains of the Zn-3Mg alloy (mean size: 1.68 μm) were significantly refined, as compared to those of the pure Zn (mean size: 40.42 μm). An increased number of grain boundaries hinder the movement of dislocations. The grain refinement strengthening can be expressed by the Hall-Petch equation [1-3]:

$$\sigma_g = k_d d^{-\frac{1}{2}} \tag{3}$$

where k_d is the strengthening coefficient (110 $MPa \cdot \mu m^{1/2}$) [44], d is the average grain size of the Zn-3Mg alloy (~1.68 μm). The contribution from the grain refinement strengthening is 87 MPa.

The precipitation strengthening is mainly controlled by the Orowan dislocation bypassing or shearing mechanism. Moving dislocations under stress will either bypass or shear second phase particles, which can be described as:

$$\sigma_s = \frac{M\mu b}{L} \tag{4}$$

where μ is the shear modulus (39.5 GPa) [45], b is the Burgers vector (0.266 nm) [46], and L is the average size of precipitated phase particles (~75 nm), which was obtained from TEM images (Fig. 2(q, t)), M (3.17) is the Taylor factor for the basal texture of the Zn-3Mg alloy (Figure S2). The calculated strengthening value of σ_s is 444 MPa.

Internal stresses, depending on dislocation density and arrangement, can be generated due to rapid solidification involved in LPBF. Dislocation strengthening can be expressed by the Bailey-Hirsch relation [47]:

$$\sigma_d = \alpha M b G \sqrt{\rho} \tag{5}$$

where α is the dislocation interaction constant (0.2) [48], ρ is the dislocation density according to the EBSD analysis (the geometrically necessary dislocation (GND) density [49], $\rho_{GND} \approx 10^{14}\ m^{-2}$ (Figure S3)). The calculated strengthening value from the σ_d is 66 MPa. The total contribution from σ_g, σ_s and σ_d is 597 MPa, which is close to the compressive yield strength values experimentally determined in this work.

The high compressive mechanical properties of the LPBF bulk Zn-3Mg alloy provided us with ample room to introduce porosity to form bone scaffolds. We, therefore, designed and printed two types of functionally gradient structures with 60 % porosity based on the diamond and gyroid unit cells, which enveloped the solid core (Fig. 1f). As suggested by Kang *et al.* [50], the porous outer layer is expected facilitate the interlocking of the orthopedic scaffold with the surrounding bone tissue and the dense region in the center to provide mechanical strength during the healing process. It is important to note that the designs created in the present research did not take the shape and dimensions of bone defects into consideration. Clinically relevant scaffold designs are deemed to be anatomic location-dependent and far more complex in geometry. Both diamond and gyroid functionally graded specimens showed significantly increased compressive yield strengths (129.34 ± 8.21 MPa and 170.75 ± 6.43 MPa, respectively) and elastic moduli (21.63 ± 1.51 GPa and 20.34 ± 0.83 GPa, respectively), which are much higher than the values reported for biodegradable porous metals and their alloys in the literature (Fig. 11a, b) [11,18,21,22,51-62]. The achieved compressive properties of the functionally graded LPBF Zn-3Mg scaffolds were comparable to those of the human cortical bone [63], endowing them with unprecedented potential for the treatment of load-bearing large bone defects. On this basis, topological designs could be applied to this alloy to fine-tune its mechanical properties further in the future [64,65].

4.3. Biodegradation performance

The biodegradation rate of ideal bone scaffolds should match the bone healing process. Since bone healing rate may vary at different locations in different patients, it is important to be able to control the biodegradation rate of LPBF Zn alloys. According to the fitted data of the equivalent circuits, the biocorrosion resistance of the materials can be ranked by the sum of R_f and R_{ct} as: V400>V800>V600>Zn (Table 3). In the low frequency region of the Nyquist plots, the lines of all the specimens were close to 45°, indicating that the diffusion process hindered the corrosion of the LPBF Zn and Zn-3Mg alloy. As indicated by the PDP curves (Fig. 5d), the Zn and Zn-3Mg specimens exhibited similar passivation behaviors in the anode region, suggesting the formation of a biodegradation film [66]. The breakdown potential values of the V600 and V800 specimens were higher than those of the V400 and Zn specimens, suggesting that V400 and Zn were more prone to localized degradation due to the disruption of the protective layers [67]. Since there is no obvious Tafel region in the anode region, the electrochemical parameters were obtained from the cathode region. The trend of i_{corr} is consistent with the EIS results that the Zn-3Mg alloy exhibits enhanced corrosion resistance as com-

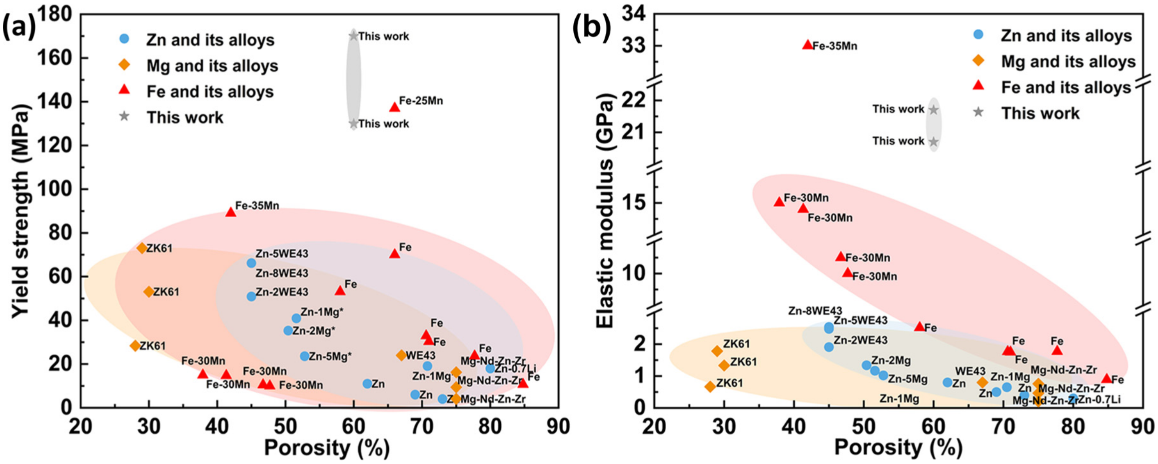

Fig. 11. Mechanical properties of the LPBF functionally graded Zn-3Mg scaffolds: (a) yield strengths *versus* porosity and (b) elastic moduli *versus* porosity – data collected from the current work and from the literature [11,18,21,22,47-58] (* represents ultimate compressive strength).

pared to pure Zn. The V600 specimens (with a corrosion rate of 0.48 mm/year) had an i_{corr} value that was almost twice as much as the i_{corr} value of the V400 specimens (0.26 mm/year) (Table 4). Since electrochemical tests only reveal the transient corrosion behavior of a metal, long-term immersion tests are needed to complement the results obtained from electrochemical tests. From the weight loss measurements, the LPBF Zn specimens showed higher *in vitro* biodegradation rates than the LPBF Zn-3Mg specimens at all the selected immersion time points.

The biodegradation behavior of a LPBF metal can be affected by many factors, such as chemical composition, microstructure, and the environment [68]. It has been reported that the addition of Mg to Zn may have dual effects on the biodegradation behavior of Zn alloys [69]. Since the standard electrochemical potential of Mg (−2.372 V) is much lower than that of Zn (−0.763 V) [70], the addition of Mg to Zn is expected to decrease its electrochemical potential. However, the solid solubility of Mg in Zn is only 0.006 wt% at 200 °C [28] and most of Mg is present in the eutectic α-Zn+Mg_2Zn_{11} phases. This explains the observation that the differences in OCP were not marked between the Zn and Zn-3Mg specimens.

In general, a reduction in grain size leads to an increase in the number of grain boundaries, thereby increasing the corrosion, as reported by Gollapudi et al. [71]:

$$i_{corr} = A + B\left(\bar{d}\right)^{-\frac{1}{2}} \exp\left(-\frac{9}{8}\right)S_n^2 \tag{6}$$

where i_{corr} is the corrosion current while A and B are two constants dependent on the material composition or impurity level, $\bar{d}$ is the average grain size, and S_n^2 is the grain size distribution. The LPBF specimens were found to have smaller grain sizes due to high-rate cooling occurring during LPBF. They could, therefore, be expected to be more susceptible to corrosion. For biodegradable metals, however, large amounts of biodegradation products form on the surface, which can act as barriers to further corrosion and, thus, reduce the biodegradation rate. For instance, Gollapudi et al. [71] have reported that a reduction in the grain size of Mg through equal channel annular pressing (ECAP) results in the formation of a compact protective layer composed of $Mg(OH)_2$ and MgO corrosion products, thereby reducing the corrosion rate in the 0.1 M NaCl solution. Zinc-based alloys are expected to exhibit similar corrosion behaviors in relation to the grain size.

Second phase dispersed in the matrix of an alloy plays an important role in determining its biodegradation rate. Depending on its OCP, sizes, and distribution, the second phase may act as a cathode to accelerate the biodegradation of the matrix or as a barrier to slow down degradation. For example, Yu et al. [72] have found in their study on a Mg-Zn-Ca alloy that the biodegradation rate increases with the second phase content while Zhou et al. [73] report that a homogeneous distribution of the β-$Mg_{17}Al_{12}$ second phase in the AZ91 magnesium alloy actually reduces the biodegradation rate.

Additional factors, such as grain orientation [74,75], residual stress [71], and specific surface area, can affect the biodegradation rates of biodegradable metals as well [76-79]. Changing the LPBF process parameters may further influence the grain orientation, anisotropy [10], morphology, number density and distribution of the second phase, and residual stresses developed in the resulting material. However, the mechanisms through which the parameters of the LPBF process affect the biodegradation process are highly complex and require separate investigations.

In this study, the corrosion resistance of the LPBF Zn-3Mg alloy was greater than that of the LPBF Zn. The dispersed fine Mg_2Zn_{11} phase acted as the cathode, forming a number of micro-galvanic couplings with the α-Zn matrix [80], which is expected to enhance the corrosion of the α-Zn matrix. On the other hand, the formation and deposition of the biodegradation products is expected to accelerate on the Zn-3Mg specimens, which translates to lower biodegradation rates for longer immersion times. The influence of the dispersed Mg_2Zn_{11} phase may be greater than the effect of grain refinement.

The biodegradation rate gradually decreased from day 1 to day 28 (Fig. 7f), most likely due to the continued deposition of the biodegradation products. As is clear from the XRD and XPS analyses, the biodegradation products were composed of hydroxides, carbonates, and phosphates, which could work as a passive film, protecting the α-Zn matrix from further degradation [49]. It can be seen from the EDS results (Fig. 6d) that the Ca, P, and O contents of the biodegradation products present on the specimen surfaces gradually increase with the immersion time, which suggest the continued deposition of hydroxyapatite-like inorganic compounds on those surfaces [62]. It is, however, important to realize that the passivation film can breakdown or peel off due to localized chemical attack or mechanical damage. When the breakdown and formation of the film reaches a dynamic equilibrium, the biodegradation rate tends to be stable.

The diamond functionally graded specimens had a higher degradation rate than the gyroid ones, which could be contributed to the higher permeability of the diamond structure. Besides the material itself, the topological design could indeed be used as an effective tool to adjust the degradation rate of biodegradable Zn-based alloy scaffolds [81].

4.4. Biocompatibility

Much previous research has already demonstrated the suitability of Zn alloys for potential use as biodegradable metallic materials. Preliminary *in vitro* and *in vivo* results all show that Zn alloys have moderate biodegradation rates and play an important role in promoting new bone formation and remodeling [82]. The alloying element Mg is an essential element for human bone health. Mg^{2+} can induce local neurons to produce calcitonin gene-related polypeptide-α (CGRP) to improve fracture healing [83,84].

We evaluated the biocompatibility of the LPBF Zn-3Mg alloy by performing indirect cytocompatibility tests according to ISO 10,993 [85]. The cells cultured with the 10 %- and 20 %-diluted extracts showed increased cell viability from day 1 to day 3, suggesting that Zn^{2+} and Mg^{2+} could, indeed, promote the proliferation of the MC3T3 cells. The 10 %-diluted extracts had a higher cell viability than the 20 %-diluted extracts, which could be attributed to a higher Zn^{2+} concentration in the latter. According to the findings of Yamamoto et al. [86], the inhibitive concentration (IC_{50}) of $ZnCl_2$ for MC3T3-E1 cells was 90 µmol/L. Townend et al. [87] have found that when Zn^{2+} concentration is greater than 80 – 120 µmol/L, the adhesion, proliferation, and migration of endothelial cells are inhibited. From the ICP analysis of the 100 % extracts, it appeared that the Zn^{2+}concentrations in the extracts of both the Zn and Zn-3Mg specimens were beyond 200 µmol/L. However, since the biodegradation products could be metabolized or be transported away *in vivo*, 9-time to 14-time dilution has been recommended for evaluating the biocompatibility of biodegradable metals [88]. The 10 %-diluted extracts were in line with this recommendation, while the 20 %-diluted extracts provided an even harsher environment for the cells. Moreover, the biocompatibility of the LPBF Zn-3Mg alloy can be affected by the parameters of the LPBF process. That is because the processing parameters can influence the biodegradation rate of the Zn-3Mg alloy and change the osmotic pressure of the medium. Zhang et al. [89] have found that an increase in osmotic pressure creates a slight inhibitory effect on the proliferation of osteoblasts, while a proper alkaline environment promotes the growth of osteoblasts. The V600 specimens showed better cell viability than the V400 and V800 specimens, which may be caused by higher Zn^{2+} and Mg^{2+} concentrations, as well as osmotic pressure. The functionally graded designs showed no adverse effect on the biocompatibility of the LPBF Zn-3Mg alloy scaffolds compared to the bulk ones.

To further investigate the effects of adding Mg to Zn on the osteogenesis of the MC3T3-E1 cells, both quantitative and qualitative ALP and AR tests were carried out. ALP is the early marker of osteoblast differentiation, while the mineralized noduli from AR are the indicator of osteoblast differentiation and maturation. For both of the LPBF materials, ALP activity increased from day 14 to day 21, while the Zn-3Mg specimens had higher ALP activity values than the pure Zn specimens, meaning that the Zn-3Mg specimens could better promote osteoblast differentiation. Similarly, the Zn-3Mg alloy showed higher AR absorbance than the pure Zn and both of the materials had higher AR absorbance values than the control group, indicating that both Zn and Zn-3Mg could stimulate the mineralization of MC3T3-E1 cell matrix, thereby increasing the anabolic activity in bone metabolism.

5. Conclusions

The LPBF Zn-3Mg alloy showed a great potential to be developed further as a biodegradable metal for the treatment of load-bearing bone defects. The parameters of the LPBF process could be used as an effective means to fine-tune the properties of biodegradable Zn alloys.

(1) Alloying Zn with Mg led to grain refinement. LPBF created a unique microstructure with the interlaced α-Zn and Zn/Mg_2Zn_{11} eutectic phases in the Zn-3Mg alloy.
(2) The LPBF Zn-3Mg alloy exhibited a peculiar tension-compression yield asymmetry. Its compressive yield strength could reach 601 MPa and its failure strain could go far beyond 60 %. Its tensile properties could be adjusted by changing the LPBF process parameters while the effect on its compressive strength was limited. Functionally graded Zn-3Mg scaffolds with a designed porosity of 60 % were developed and exhibited compressive yield strengths higher than 120 MPa, satisfying the mechanical strength requirement for the repair of load-bearing bone defects.
(3) The addition of Mg to Zn decreased the biodegradation rate of Zn while the biodegradation rate of the LPBF Zn-3Mg alloy could be regulated by tuning the parameters of the LPBF process.
(4) The LPBF Zn-3Mg alloy showed improved biocompatibility as compared to the LPBF pure Zn. Different LPBF parameters could cause differences in cytocompatibility and osteogenic properties as well.

Declaration of competing interest

The authors declare that they have no known competing financial interests or personal relationships that could have appeared to influence the work reported in this paper.

CRediT authorship contribution statement

Yuzhe Zheng: Writing – original draft, Methodology, Investigation, Formal analysis, Data curation, Conceptualization. **Chengcong Huang:** Writing – original draft, Methodology, Investigation, Data curation. **Yageng Li:** Writing – review & editing, Writing – original draft, Validation, Supervision, Resources, Project administration, Investigation, Funding acquisition, Conceptualization. **Jiaqi Gao:** Methodology, Investigation. **Youwen Yang:** Writing – review & editing, Methodology. **Shangyan Zhao:** Methodology, Investigation. **Haodong Che:** Methodology, Investigation. **Yabin Yang:** Writing – review & editing, Methodology, Investigation. **Shenglian Yao:** Writing – review & editing, Methodology. **Weishi Li:** Writing – review & editing, Methodology. **Jie Zhou:** Writing – review & editing, Methodology, Formal analysis. **Amir A. Zadpoor:** Writing – review & editing, Methodology, Formal analysis. **Luning Wang:** Writing – review & editing, Writing – original draft, Supervision, Resources, Project administration, Formal analysis, Conceptualization.

Acknowledgments

The work was financially supported by supported by the National Key Research & Development Program of China (No. 2023YFB3813000), the National Natural Science Foundation of China (52201294, 52231010, 52071028, 52105421), China Postdoctoral Science Foundation (2022M710345), Natural Science Foundation of Beijing (L212014), Beijing Nova Program (2022 Beijing Nova Program Cross Cooperation Program No. 20220484178), Fundamental Research Funds for the Central Universities and the Youth Teacher International Exchange & Growth Program (No. QNXM20220022), and Guangdong Provincial Natural Science Foundation (No. 2022A1515011621).

Supplementary materials

Supplementary material associated with this article can be found, in the online version, at doi:10.1016/j.actbio.2024.05.023.

References

[1] Y. Li, H. Jahr, J. Zhou, A.A. Zadpoor, Additively manufactured biodegradable porous metals, Acta Biomater. 115 (2020) 29–50.

[2] M.-M. Germaini, S. Belhabib, S. Guessasma, R. Deterre, P. Corre, P. Weiss, Additive manufacturing of biomaterials for bone tissue engineering – A critical review of the state of the art and new concepts, Prog. Mater Sci. 130 (2022) 100963.

[3] S.M. Ahmadi, R. Hedayati, Y. Li, K. Lietaert, N. Tümer, A. Fatemi, C.D. Rans, B. Pouran, H. Weinans, A.A. Zadpoor, Fatigue performance of additively manufactured meta-biomaterials: the effects of topology and material type, Acta Biomater. 65 (2018) 292–304.

[4] R. Hedayati, S.M. Ahmadi, K. Lietaert, B. Pouran, Y. Li, H. Weinans, C.D. Rans, A.A. Zadpoor, Isolated and modulated effects of topology and material type on the mechanical properties of additively manufactured porous biomaterials, J. Mech. Behav. Biomed. Mater. 79 (2018) 254–263.

[5] G. Li, L. Zhang, L. Wang, G. Yuan, K. Dai, J. Pei, Y. Hao, Dual modulation of bone formation and resorption with zoledronic acid-loaded biodegradable magnesium alloy implants improves osteoporotic fracture healing: an *in vitro* and *in vivo* study, Acta Biomater. 65 (2018) 486–500.

[6] C. Garot, G. Bettega, C. Picart, Additive manufacturing of material scaffolds for bone regeneration: toward application in the clinics, Adv. Funct. Mater. 31 (5) (2021) 2006967.

[7] J.-L. Wang, J.-K. Xu, C. Hopkins, D.H.-K. Chow, L. Qin, Biodegradable magnesium-based implants in orthopedics—a general review and perspectives, Adv. Sci. 7 (8) (2020) 1902443.

[8] Y. Shi, Z. Xue, P. Li, S. Yang, D. Zhang, S. Zhou, Z. Guan, Y. Li, L.-N. Wang, Surface modification on biodegradable zinc alloys, J. Mater. Res. Technol. 25 (2023) 3670–3687.

[9] J.P. O'Connor, D. Kanjilal, M. Teitelbaum, S.S. Lin, J.A. Cottrell, Zinc as a therapeutic agent in bone regeneration, Materials 13 (10) (2020) 2211.

[10] J. Venezuela, M.S. Dargusch, The influence of alloying and fabrication techniques on the mechanical properties, biodegradability and biocompatibility of zinc: a comprehensive review, Acta Biomater. 87 (2019) 1–40.

[11] Y. Li, H. Jahr, K. Lietaert, P. Pavanram, A. Yilmaz, L.I. Fockaert, M.A. Leeflang, B. Pouran, Y. Gonzalez-Garcia, H. Weinans, J.M.C. Mol, J. Zhou, A.A. Zadpoor, Additively manufactured biodegradable porous iron, Acta Biomater. 77 (2018) 380–393.

[12] Y. Li, K. Lietaert, W. Li, X.Y. Zhang, M.A. Leeflang, J. Zhou, A.A. Zadpoor, Corrosion fatigue behavior of additively manufactured biodegradable porous iron, Corros. Sci. 156 (2019) 106–116.

[13] Y. Li, P. Pavanram, J. Zhou, K. Lietaert, P. Taheri, W. Li, H. San, M.A. Leeflang, J.M.C. Mol, H. Jahr, A.A. Zadpoor, Additively manufactured biodegradable porous zinc, Acta Biomater. 101 (2020) 609–623.

[14] Y. Li, P. Pavanram, J. Bühring, S. Rütten, K.U. Schröder, J. Zhou, T. Pufe, L.N. Wang, A.A. Zadpoor, H. Jahr, Physiomimetic biocompatibility evaluation of directly printed degradable porous iron implants using various cell types, Acta Biomater. 169 (2023) 589–604.

[15] M. Montani, A.G. Demir, E. Mostaed, M. Vedani, B. Previtali, Processability of pure Zn and pure Fe by SLM for biodegradable metallic implant manufacturing, Rapid Prototyp. J. 23 (3) (2017) 514–523.

[16] A.G. Demir, L. Monguzzi, B. Previtali, Selective laser melting of pure Zn with high density for biodegradable implant manufacturing, Addit. Manuf. 15 (2017) 20–28.

[17] K. Lietaert, W. Baekelant, L. Thijs, J. Vleugels, Direct metal printing of zinc: from single laser tracks to high density parts, European Congress and Exhibition on Powder Metallurgy, in: European PM Conference Proceedings, The European Powder Metallurgy Association, Swerea KIMAB, Sweden, 2016, pp. 1–6.

[18] Y. Li, J. Zhou, P. Pavanram, M.A. Leeflang, L.I. Fockaert, B. Pouran, N. Tümer, K.U. Schröder, J.M.C. Mol, H. Weinans, H. Jahr, A.A. Zadpoor, Additively manufactured biodegradable porous magnesium, Acta Biomater. 67 (2018) 378–392.

[19] Z. Shan, X. Xie, X. Wu, S. Zhuang, C. Zhang, Development of degradable magnesium-based metal implants and their function in promoting bone metabolism (A review), J. Orthop. Translat. 36 (2022) 184–193.

[20] Y. Yang, F. Yuan, C. Gao, P. Feng, L. Xue, S. He, C. Shuai, A combined strategy to enhance the properties of Zn by laser rapid solidification and laser alloying, J. Mech. Behav. Biomed. Mater. 82 (2018) 51–60.

[21] Y. Qin, A. Liu, H. Guo, Y. Shen, P. Wen, H. Lin, D. Xia, M. Voshage, Y. Tian, Y. Zheng, Additive manufacturing of Zn-Mg alloy porous scaffolds with enhanced osseointegration: *in vitro* and *in vivo* studies, Acta Biomater. 145 (2022) 403–415.

[22] M. Voshage, S. Megahed, P.G. Schückler, P. Wen, Y. Qin, L. Jauer, R. Poprawe, J.H. Schleifenbaum, Additive manufacturing of biodegradable Zn-xMg alloys: effect of Mg content on manufacturability, microstructure and mechanical properties, Mater. Today Commun. 32 (2022) 103805.

[23] Y. Li, J. Shi, H. Jahr, J. Zhou, A.A. Zadpoor, L. Wang, Improving the mechanical properties of additively manufactured micro-architected biodegradable metals, JOM 73 (12) (2021) 4188–4198.

[24] J. Ning, Z.-X. Ma, L.-J. Zhang, D.-P. Wang, S.-J. Na, Effects of magnesium on microstructure, properties and degradation behaviors of zinc-based alloys prepared by selective laser melting, Mater. Res. Express 9 (8) (2022) 086511.

[25] M.S. Dambatta, S. Izman, D. Kurniawan, S. Farahany, B. Yahaya, H. Hermawan, Influence of thermal treatment on microstructure, mechanical and degradation properties of Zn–3Mg alloy as potential biodegradable implant material, Mater. Des. 85 (2015) 431–437.

[26] F. An, Z. Ma, K. Sun, L. Zhang, S.J. Na, J. Ning, H. Yu, Influences of the Ag content on microstructures and properties of Zn–3Mg–xAg alloy by spark plasma sintering, J. Mater. Res. Technol. 24 (2023) 595–607.

[27] ASTM G31-72: Standard Practice for Laboratory Immersion Corrosion Testing of MetalsAnnual Book of ASTM standards, American Society for Testing and Materials, Filadelfia, Pennsylvania, 2004.

[28] H. Jin, S. Zhao, R. Guillory, P.K. Bowen, Z. Yin, A. Griebel, J. Schaffer, E.J. Earley, J. Goldman, J.W. Drelich, Novel high-strength, low-alloys Zn-Mg (<0.1wt% Mg) and their arterial biodegradation, Mater. Sci. Eng., C 84 (2018) 67–79.

[29] T. Mukherjee, J.W. Elmer, H.L. Wei, T.J. Lienert, W. Zhang, S. Kou, T. DebRoy, Control of grain structure, phases, and defects in additive manufacturing of high-performance metallic components, Prog. Mater Sci. 138 (2023) 101153.

[30] C. Yao, Z. Wang, S.L. Tay, T. Zhu, W. Gao, Effects of Mg on microstructure and corrosion properties of Zn–Mg alloy, J. Alloys Compd. 602 (2014) 101–107.

[31] C. Wang, Y. Hu, C. Zhong, C. Lan, W. Li, X. Wang, Microstructural evolution and mechanical properties of pure Zn fabricated by selective laser melting, Mater. Sci. Eng., A 846 (2022) 143276.

[32] P. Wen, Y. Qin, Y. Chen, M. Voshage, L. Jauer, R. Poprawe, J.H. Schleifenbaum, Laser additive manufacturing of Zn porous scaffolds: shielding gas flow, surface quality and densification, J. Mater. Sci. Technol. 35 (2) (2019) 368–376.

[33] T. DebRoy, H.L. Wei, J.S. Zuback, T. Mukherjee, J.W. Elmer, J.O. Milewski, A.M. Beese, A. Wilson-Heid, A. De, W. Zhang, Additive manufacturing of metallic components – process, structure and properties, Prog. Mater Sci. 92 (2018) 112–224.

[34] X. Yuan, M. Liu, K. Wei, F. Li, X. Li, X. Zeng, Defect, microstructure and mechanical properties of Mg–Gd binary alloy additively manufactured by selective laser melting, Mater. Sci. Eng. A 850 (2022) 143572.

[35] Y. Qin, P. Wen, D. Xia, H. Guo, M. Voshage, L. Jauer, Y. Zheng, J.H. Schleifenbaum, Y. Tian, Effect of grain structure on the mechanical properties and *in vitro* corrosion behavior of additively manufactured pure Zn, Addit. Manuf. 33 (2020) 101134.

[36] L. Ye, H. Huang, C. Sun, X. Zhuo, Q. Dong, H. Liu, J. Ju, F. Xue, J. Bai, J. Jiang, Effect of grain size and volume fraction of eutectic structure on mechanical properties and corrosion behavior of as-cast Zn–Mg binary alloys, J. Mater. Res. Technol. 16 (2022) 1673–1685.

[37] C.S. Pande, K.P. Cooper, Nanomechanics of Hall–Petch relationship in nanocrystalline materials, Prog. Mater Sci. 54 (6) (2009) 689–706.

[38] C. Chen, H. Huang, J. Niu, J.-F. Nie, G. Yuan, Origin of high tension-compression yield asymmetry in as-extruded pure zinc, Scr. Mater. 200 (2021) 113922.

[39] H.F. Li, X.H. Xie, Y.F. Zheng, Y. Cong, F.Y. Zhou, K.J. Qiu, X. Wang, S.H. Chen, L. Huang, L. Tian, L. Qin, Development of biodegradable Zn-1X binary alloys with nutrient alloying elements Mg, Ca and Sr, Sci. Rep 5 (2015) 10719.

[40] X. Tong, W. Cai, J. Lin, K. Wang, L. Jin, Z. Shi, D. Zhang, J. Lin, Y. Li, M. Dargusch, C. Wen, Biodegradable Zn−3Mg−0.7Mg2Si composite fabricated by high-pressure solidification for bone implant applications, Acta Biomater. 123 (2021) 407–417.

[41] X. Lv, Crack initiation considering the possible stress acting on the crack surface under uniaxial tension or compression, Theor. Appl. Fract. Mech. 121 (2022) 103433.

[42] Y.-P.R. Li-Qing Wang, S.-N. Sun, H. Zhao, S. Li, G.-W. Qin, Microstructure, mechanical properties and fracture behavior of as-extruded Zn-Mg binary alloys, Acta Metall. Sin. 30 (10) (2017) 931–940.

[43] D. Nečas, I. Marek, J. Pinc, D. Vojtěch, J. Kubásek, Advanced zinc–magnesium alloys prepared by mechanical alloying and spark plasma Sintering, Materials 15 (15) (2022) 5272.

[44] D. Liang, C. Wei, F. Ren, Introducing Laves phase strengthening into an ultra-fine-grained equiatomic CrFeNi alloy by niobium addition, Mater. Sci. Eng., A 806 (2021) 140611.

[45] R.V. Goldstein, V.A. Gorodtsov, M.A. Komarova, D.S. Lisovenko, Extreme values of the shear modulus for hexagonal crystals, Scr. Mater. 140 (2017) 55–58.

[46] M.D. Sangid, T. Ezaz, H. Sehitoglu, Energetics of residual dislocations associated with slip–twin and slip–GBs interactions, Mater. Sci. Eng., A 542 (2012) 21–30.

[47] J.E. Bailey, P.B. Hirsch, The dislocation distribution, flow stress, and stored energy in cold-worked polycrystalline silver, Philos. Mag. 5 (53) (1960) 485–497.

[48] E. Khafizova, E. Fakhretdinova, R. Islamgaliev, M. Polenok, V. Sitdikov, H. Yilmazer, Effect of plastic deformation on the structure and mechanical properties of the Zn-4Ag-1Cu Zinc alloy, Materials 16 (13) (2023) 4646.

[49] M. Calcagnotto, D. Ponge, E. Demir, D. Raabe, Orientation gradients and geometrically necessary dislocations in ultrafine grained dual-phase steels studied by 2D and 3D EBSD, Mater. Sci. Eng., A 527 (10) (2010) 2738–2746.

[50] M.-H. Kang, H. Lee, T.-S. Jang, Y.-J. Seong, H.-E. Kim, Y.-H. Koh, J. Song, H.-D. Jung, Biomimetic porous Mg with tunable mechanical properties and biodegradation rates for bone regeneration, Acta Biomater. 84 (2019) 453–467.

[51] A. Kopp, T. Derra, M. Müther, L. Jauer, J.H. Schleifenbaum, M. Voshage, O. Jung, R. Smeets, N. Kröger, Influence of design and postprocessing parameters on the degradation behavior and mechanical properties of additively manufactured magnesium scaffolds, Acta Biomater. 98 (2019) 23–35.

[52] F. Witte, L. Jauer, W. Meiners, Z. Kronbach, K. Strohschein, T. Schmidt, Open–porous biodegradable magnesium scaffolds produced by selective laser melting for individualized bone replacement, Front. Bioeng. BioTech. 4 (2016).

[53] M. Salehi, S. Maleksaeedi, M.A.B. Sapari, M.L.S. Nai, G.K. Meenashisundaram, M. Gupta, Additive manufacturing of magnesium–zinc–zirconium (ZK) alloys via capillary-mediated binderless three-dimensional printing, Mater. Des. 169 (2019) 107683.

[54] C. Shuai, W. Yang, Y. Yang, H. Pan, C. He, F. Qi, D. Xie, H. Liang, Selective laser melted Fe-Mn bone scaffold: microstructure, corrosion behavior and cell response, Mater. Res. Express 7 (1) (2020) 015404.

[55] D. Carluccio, C. Xu, J. Venezuela, Y. Cao, D. Kent, M. Bermingham, A.G. Demir, B. Previtali, Q. Ye, M. Dargusch, Additively manufactured iron-manganese for biodegradable porous load-bearing bone scaffold applications, Acta Biomater. 103 (2020) 346–360.

[56] Y. Li, H. Jahr, P. Pavanram, F.S.L. Bobbert, U. Puggi, X.Y. Zhang, B. Pouran, M.A. Leeflang, H. Weinans, J. Zhou, A.A. Zadpoor, Additively manufactured functionally graded biodegradable porous iron, Acta Biomater. 96 (2019) 646–661.

[57] Y. Yang, Y. Cheng, S. Peng, L. Xu, C. He, F. Qi, M. Zhao, C. Shuai, Microstructure evolution and texture tailoring of reduced graphene oxide reinforced Zn scaffold, Bioact. Mater. 6 (5) (2021) 1230–1241.

[58] Y. Qin, H. Yang, A. Liu, J. Dai, P. Wen, Y. Zheng, Y. Tian, S. Li, X. Wang, Processing optimization, mechanical properties, corrosion behavior and cytocompatibility of additively manufactured Zn-0.7Li biodegradable metals, Acta Biomater. 142 (2022) 388–401.

[59] H. Hyer, L. Zhou, Q. Liu, D. Wu, S. Song, Y. Bai, B. McWilliams, K. Cho, Y. Sohn, High strength WE43 microlattice structures additively manufactured by laser powder bed fusion, Materialia 16 (2021) 101067.

[60] B. Yin, J. Liu, B. Peng, M. Zhou, B. Liu, X. Ma, C. Wang, P. Wen, Y. Tian, Y. Zheng, Influence of layer thickness on formation quality, microstructure, mechanical properties, and corrosion resistance of WE43 magnesium alloy fabricated by laser powder bed fusion, J. Magnes. Alloy (2022).

[61] Y. Wang, P. Fu, N. Wang, L. Peng, B. Kang, H. Zeng, G. Yuan, W. Ding, Challenges and solutions for the additive manufacturing of biodegradable magnesium implants, Engineering 6 (11) (2020) 1267–1275.

[62] Y. Li, P. Pavanram, J. Zhou, K. Lietaert, F.S.L. Bobbert, Y. Kubo, M.A. Leeflang, H. Jahr, A.A. Zadpoor, Additively manufactured functionally graded biodegradable porous zinc, Biomater. Sci. 8 (9) (2020) 2404–2419.

[63] S. Wu, X. Liu, K.W.K. Yeung, C. Liu, X. Yang, Biomimetic porous scaffolds for bone tissue engineering, Mater. Sci. Eng. R Rep. 80 (2014) 1–36.

[64] M.S. Dargusch, N. Soro, A.G. Demir, J. Venezuela, Q. Sun, Y. Wang, A. Abdal-hay, A.Q. Alali, S. Ivanovski, B. Previtali, D. Kent, Optimising degradation and mechanical performance of additively manufactured biodegradable Fe–Mn scaffolds using design strategies based on triply periodic minimal surfaces, Smart Mater. Med. 5 (1) (2024) 127–139.

[65] Y. Wang, H. Huang, G. Jia, H. Zeng, G. Yuan, Fatigue and dynamic biodegradation behavior of additively manufactured Mg scaffolds, Acta Biomater. 135 (2021) 705–722.

[66] M.A.F. Romzi, J. Alias, M.I.M. Ramli, Effect of zinc (Zn) on the microstructure and corrosion behaviour of magnesium (Mg), Mater. Today 48 (2022) 1873–1879.

[67] D. Hong, P. Saha, D.-T. Chou, B. Lee, B.E. Collins, Z. Tan, Z. Dong, P.N. Kumta, *In vitro* degradation and cytotoxicity response of Mg–4% Zn–0.5% Zr (ZK40) alloy as a potential biodegradable material, Acta Biomater.. 9 (10) (2013) 8534–8547.

[68] Y. Qin, P. Wen, H. Guo, D. Xia, Y. Zheng, L. Jauer, R. Poprawe, M. Voshage, J.H. Schleifenbaum, Additive manufacturing of biodegradable metals: current research status and future perspectives, Acta Biomater. 98 (2019) 3–22.

[69] C. Li, T. Huang, Z. Liu, Effects of thermomechanical processing on microstructures, mechanical properties, and biodegradation behaviour of dilute Zn–Mg alloys, J. Mater. Res. Technol. 23 (2023) 2940–2955.

[70] J. Kubásek, D. Vojtěch, E. Jablonská, I. Pospíšilová, J. Lipov, T. Ruml, Structure, mechanical characteristics and *in vitro* degradation, cytotoxicity, genotoxicity and mutagenicity of novel biodegradable Zn–Mg alloys, Mater. Sci. Eng., C 58 (2016) 24–35.

[71] S. Gollapudi, Grain size distribution effects on the corrosion behaviour of materials, Corros. Sci. 62 (2012) 90–94.

[72] Y. Lu, A.R. Bradshaw, Y.L. Chiu, I.P. Jones, Effects of secondary phase and grain size on the corrosion of biodegradable Mg–Zn–Ca alloys, Mater. Sci. Eng., C 48 (2015) 480–486.

[73] W. Zhou, T. Shen, N.N. Aung, Effect of heat treatment on corrosion behaviour of magnesium alloy AZ91D in simulated body fluid, Corros. Sci. 52 (3) (2010) 1035–1041.

[74] Z. Pu, G.L. Song, S. Yang, J.C. Outeiro, O.W. Dillon, D.A. Puleo, I.S. Jawahir, Grain refined and basal textured surface produced by burnishing for improved corrosion performance of AZ31B Mg alloy, Corros. Sci. 57 (2012) 192–201.

[75] J.W. Schultze, B. Davepon, F. Karman, C. Rosenkranz, A. Schreiber, O. Voigt, Corrosion and passivation in nanoscopic and microscopic dimensions: the influence of grains and grain boundaries, Corros. Eng., Sci. Technol. 39 (1) (2004) 45–52.

[76] M. Yazdimamaghani, M. Razavi, D. Vashaee, K. Moharamzadeh, A.R. Boccaccini, L. Tayebi, Porous magnesium-based scaffolds for tissue engineering, Mater. Sci. Eng., C 71 (2017) 1253–1266.

[77] W. Jin, G. Wu, H. Feng, W. Wang, X. Zhang, P.K. Chu, Improvement of corrosion resistance and biocompatibility of rare-earth WE43 magnesium alloy by neodymium self-ion implantation, Corros. Sci. 94 (2015) 142–155.

[78] Y. Li, W. Li, F.S.L. Bobbert, K. Lietaert, J.H. Dong, M.A. Leeflang, J. Zhou, A.A. Zadpoor, Corrosion fatigue behavior of additively manufactured biodegradable porous zinc, Acta Biomater. 106 (2020) 439–449.

[79] B. Wegener, B. Sievers, S. Utzschneider, P. Müller, V. Jansson, S. Rößler, B. Nies, G. Stephani, B. Kieback, P. Quadbeck, Microstructure, cytotoxicity and corrosion of powder-metallurgical iron alloys for biodegradable bone replacement materials, Mater. Sci. Eng. B 176 (20) (2011) 1789–1796.

[80] C. Shen, X. Liu, B. Fan, P. Lan, F. Zhou, X. Li, H. Wang, X. Xiao, L. Li, S. Zhao, Z. Guo, Z. Pu, Y. Zheng, Mechanical properties, *in vitro* degradation behavior, hemocompatibility and cytotoxicity evaluation of Zn–1.2Mg alloy for biodegradable implants, RSC Adv. 6 (89) (2016) 86410–86419.

[81] Y. Li, P. Pavanram, J. Zhou, K. Lietaert, F.S.L. Bobbert, Y. Kubo, M.A. Leeflang, H. Jahr, A.A. Zadpoor, Additively manufactured functionally graded biodegradable porous zinc, Biomater. Sci. (2020).

[82] D. Hernández-Escobar, S. Champagne, H. Yilmazer, B. Dikici, C.J. Boehlert, H. Hermawan, Current status and perspectives of zinc-based absorbable alloys for biomedical applications, Acta Biomater. 97 (2019) 1–22.

[83] Y. Zhang, J. Xu, Y.C. Ruan, M.K. Yu, M. O'Laughlin, H. Wise, D. Chen, L. Tian, D. Shi, J. Wang, S. Chen, J.Q. Feng, D.H.K. Chow, X. Xie, L. Zheng, L. Huang, S. Huang, K. Leung, N. Lu, L. Zhao, H. Li, D. Zhao, X. Guo, K. Chan, F. Witte, H.C. Chan, Y. Zheng, L. Qin, Implant-derived magnesium induces local neuronal production of CGRP to improve bone-fracture healing in rats, Nat. Med. 22 (10) (2016) 1160–1169.

[84] H. Zhou, B. Liang, H. Jiang, Z. Deng, K. Yu, Magnesium-based biomaterials as emerging agents for bone repair and regeneration: from mechanism to application, J. Magnes. Alloy 9 (3) (2021) 779–804.

[85] ISO, 10993-5:2009(En): Biological Evaluation of Medical Devices—Part 5: Tests for In Vitro Cytotoxicity (2009).

[86] A. Yamamoto, R. Honma, M. Sumita, Cytotoxicity evaluation of 43 metal salts using murine fibroblasts and osteoblastic cells, J. Biomed. Mater. Res. 39 (2) (1998) 331–340.

[87] M. Townend, P. Parker, Metalwork removal in potential army recruits. evidence-based changes to entry criteria, J. R. Army Med. Corps 151 (1) (2005) 2.

[88] J. Wang, F. Witte, T. Xi, Y. Zheng, K. Yang, Y. Yang, D. Zhao, J. Meng, Y. Li, W. Li, K. Chan, L. Qin, Recommendation for modifying current cytotoxicity testing standards for biodegradable magnesium-based materials, Acta Biomater. 21 (2015) 237–249.

[89] L. Zhang, J. Pei, H. Wang, Y. Shi, J. Niu, F. Yuan, H. Huang, H. Zhang, G. Yuan, Facile preparation of poly(lactic acid)/brushite bilayer coating on biodegradable magnesium alloys with multiple functionalities for orthopedic application, ACS Appl. Mater. Interfaces 9 (11) (2017) 9437–9448.